Indian J. Phys. **74B** (6), 415–444 (2000)

REVIEW

I J P B
an international journal

Nucleosynthesis involving mainly neutron capture processes IV

Ramen Kumar Parui
ACS, Imphal Airport, Tulihal, Imphal-795 140, India
E-mail rkparui@yahoo.com

Received 18 May 1998, accepted 16 March 1999

Abstract . Nucleosynthesis plays a crucial role in the physics of stellar evolution. Heavy nuclei abundances in the universe provide a concrete evidence for the operation of specific nucleosynthesis processes. The slow (s-) and rapid (r-) processes are the main processes responsible for the synthesis of nuclei beyond iron, *i.e.* synthesis of nuclei heavier than Fe by neutron capture. In the preceeding papers (Paper I [1], Paper II [2], Paper III [3]), we have reviewed important neutron capture processes in investigating the mechanism of stellar nucleosynthesis, *i.e.* various neutron producing reactions (neutron sources) during stellar nucleosynthesis in different evolving stages - main sequence stage, red giant stage, supernova stage and neutron star stage. Neutrons produced in one stage come into next stage as remnant and play an active role to begin nucleosynthesis in the next stage, and ultimately to the formation of neutron star. We have indicated various constraints and unsolved problems in each stage. With the help of advanced observational technology and numerical simulations considerable efforts have been made to resolve the unsolved problems in nuclear astrophysics in recent years. Analysis of those observed parameters may give rise to significant improvement towards understanding the physics of stellar nucleosynthesis. In the present review, we have updated our previous attempt by incorporating those significant improvements in the theory of neutron capture nucleosynthesis based upon observations, theoretical calculations and numerical simulations.

Keywords Nucleosynthesis, supernova remnants, neutron star

PACS Nos. 26.30.+k, 98.38.Mz, 97.60.Jd

Plan of the Article

1. Introduction

Study of nucleosynthesis provides information for understanding the physics of stellar evolution, origin of the elements in stars, nuclear synthesis as well as generation of heavy elements during stellar evolution. It is understood from the analysis of abundance curve of the nuclei found in nature that the nuclei inside the stars are the product of a sequence of more or less discrete processes with an indication of the formation of heavier nuclei than Fe by neutron captures. Depending upon the time scales for neutron captures this may take place either before or after beta-decay of the seed nuclei [4]. Two major distinct contributors to the neutron capture are the s-process (slow neutron capture process) and the r-process (rapid neutron capture process). The s-process takes place on a long time scale (of the order of months and years) when neutron density is low and the temperature is much less than 10^9 K, while the r-process takes place for a very high neutron density and temperature in excess of 10^9 K, an environment which does not allow the seed to beta-decay nuclei. More precisely, the typical neutron density required for the operation of s-process is in the range of 10^7–10^9 cm^{-3}, with the required temperature in excess of 10^8 K [5]. However, considering the necessary nuclear physics input in astrophysical environment, it has been found in a purely phenomenological approach that the abundance of s-process nucleides is very much satisfactory, while the r-process definitely requires a neutron density in the range of 10^{20}–10^{30} cm^{-3} and a temperature in excess of 10^9 K [6]. Secondly, as the s-process more or less takes place along the line of β-stability, the β-stability line plays a crucial role not only in building up of heavy nuclei but also for the information on neutron availability during the synthesis of heavy nuclei. Thirdly, the recent abundance curve (see Figure 1 and Figure 2 in paper III) analysis indicates that although the s-process is the major distinct nucleosynthetic process occurring in an environment with a much lower neutron density than the r-process requirement, it does not freeze out from the equilibrium. This means that the s-process fails to achieve the equilibrium though the conditions favour this to take place. One of the main reasons is the production of s-nuclei by the pre-existing seed nuclei through the capture of liberated neutrons during the reaction. This indicates that the environment of star formation region as well as the surroundings may somehow be important for throwing light on this matter. Recent analysis [7] of solar system s-process abundance suggests two components of the s-process namely, (a) the main or strong s-process component - having neutron exposure with $\tau_0 \approx 0.30$ mb^{-1} which produces most of the nuclei in the mass range $90 < A \leq 204$; (b) a weak s-process component - having neutron exposure with $\tau_0 \approx 0.60$ mb^{-1} which produces nuclei for $A \leq 90$. This analysis also indicates that it is very difficult to separate the $A \leq 90$ s-nuclei produced through the weak component from the s-nuclei coming from main components. The important point is that the neutron density *i.e.*, the supply of neutrons to run the s-process, is affected by several light elements known as "poison". For example, ^{22}Ne is itself a potential poison in helium burning *via* the reaction ^{22}Ne(n,γ)^{23}Ne which was first considered by Truran and Iben [8]. A lot of measurements of the cross section of this reaction have been done but uncertainty still remains [9]. This information is vital in order to settle the neutron densities and non-solar abundance at the branches along the s-process path.

In a r-process, the nature of the reaction, *i.e.*, whether it is a primary or a secondary one, is also important for determining its occurrence as well as its duration. Although the time scales associated with the r-process are very much short generally causing violent events (for example, primary r-process such as supernova, winds from nascent neutron star, *etc*) this can still occurs slowly in a neutron rich system. For a primary r-process, the required neutron abundance depends directly on the entropy per baryon. In a high entropy environment, the necessary neutron abundance is less than that in a low entropy system. However, for a low entropy environment Wilson and Mayle [10], and Woosley *et al* [11] suggested that the r-process needs an electron fraction Y_e as low as 0.1–0.2 at the boundary between the matter that escapes into space from supernova and the matter that remains as part of the remnant neutron star. This value is inconsistent with the presently accepted value of Y_e (*e.g.*, the yield of Y_e from type II supernova is more than expected). One of the possible reasons for this difficulty is the appearence of winds from the nascent neutron stars due to r-process. Another major difficulty is that the observations of most of the r-process elements in this dominant state of ionization are at optical wavelengths [12]. So, a full survey of stellar nucleosynthesis is very much required to understand the above problem.

The main aim of this review is to give a broad view of various neutron capture processes during stellar evolution to the readers so that they can get an idea of the physics of nucleosynthesis involving mainly neutron capture. In this final review we have presented neutron capture nucleosynthesis involving s-, p-, and r-processes occurring at various stages during stellar evolution *i.e.* from the birth of a star to its neutron star stage. The paper is arranged in the following manner :

In Section 2, we have discussed the latest available abundances pointing out new probable sites for s- and r-processes. We have overviewed in Section 3 the earlier difficulties that existed in different phases of stellar evolution indicating various unsolved problems which need further attention. A progress report of the latest developments achieved through observations, theoretical calculations and numerical simulations is presented in Section 4. The Section

on "conclusion and outlook" is devoted mainly to various unsolved problems remaining for future investigation. It is hoped that a table of unsolved problems of neutron capture nucleosynthesis presented in this Section will provide the readers the modern perspective and perhaps give some directions for future study to unlock the physics of neutron capture nucleosynthesis for a full understanding.

2. Abundances

The analysis of abundance pattern observed in nature provides us the information about nucleosynthesis that is taking place in the interior of a star during its evolution. As most of the heavy elements (*i.e.*, heavier than iron peak) are synthesized to various degree inside the star by the two main mechanisms, namely, s-process and r-process, the relative contribution of s-process as well as r-process to any of these elements can be analyzed from the observed abundance curve. Not only that, a comparison of the isotopic abundances of these elements in the solar system materials with the theoretically predicted s-process model allows us to determine the degree of synthesis of different isotopes produced by these two processes. Figure 1 shows the recent abundance curve, schematically decomposed into s-process, r-process, p-process and other contributions as a function of atomic mass number (A). The s-nuclei abundance distribution exhibits peaks around the mass numbers 87, 138 and 208 while r-nuclei abundance distribution shows the peaks at the mass numbers 80, 130 and 195.

2.1 s-process

In paper I (see Figure 3), we have indicated the possible neutron capture path for s-process. The discovery of technetium and its isotopes in stars (sub-class of red giant) confirms occurrence of the s-process in the helium burning stage of stellar evolution. This also indicates that in the helium burning zone the neutrons for the s-process are supplied by the predominant (α,n) reaction on the isotopes ^{13}C and ^{22}Ne with the usual assumption that a small fraction of the observed ^{56}Fe abundance is available as a seed in this stage. With this classical approach, the behaviour of the s-process of neutron capture nucleosynthesis can successfully explain the observed abundances produced during the helium burning phase in the red giant stars with typical uncertainties of 3% [15]. But the observed abundances, in general, are the contributions from both s- and r- neutron capture processes. As the occurrence of r-process requires extremely high neutron density, the synthesis path shifts from the valley of beta stability to the neutron rich side by about 15 to 20 mass

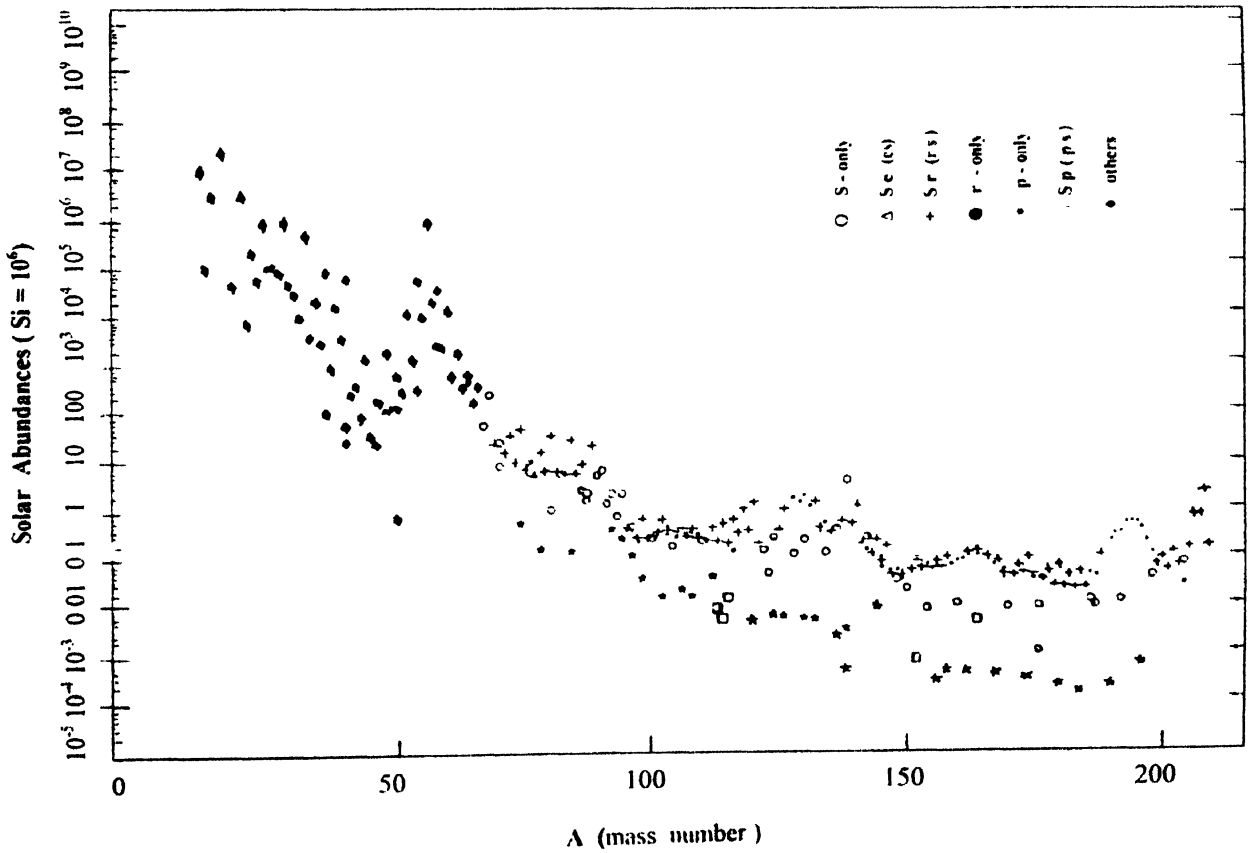

Figure 1. Recent solar system abundances relative to Si = 10^6 compiled by Anders and Grevesse [13]. Isotopes of s-nuclei, r-nuclei, p-nuclei and other nuclei are also shown (from Ref [14])

units [16] (See Figure 2). The rate of neutron capture at the s-process branching is comparable to the rate of beta decay.

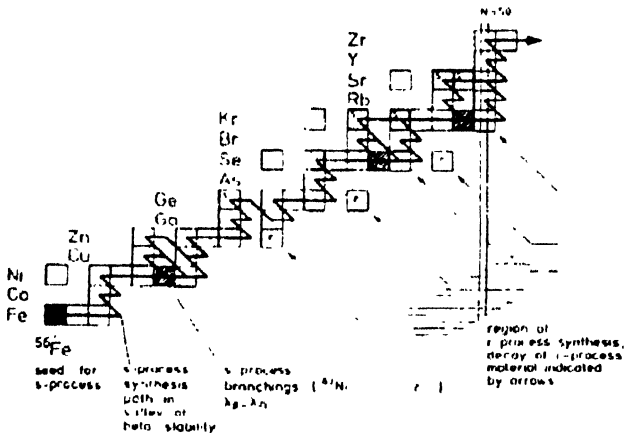

Figure 2. The synthesis path of the s-process neutron capture chain from Fe to Zr (solid line). Sufficiently long-lived isotopes which may represent potential chronometers are indicated by shaded boxes (Ref [16]).

In particular, the competition between neutron capture at ^{63}Ni, ^{79}Se and ^{85}Kr and beta decay is so high that the branching of the synthesis path is controlled by the s-process neutron density and the respective beta decay. Two possible components of s-process have been inferred from the observed abundances. The one that produces the s-abundances from zirconium to bismuth and the second one that is effective for the production of s-abundances between iron and yttrium. These two are called the main and the weak s-process components. However, detection of the s-only abundance of isotopes of tellurium *i.e.* ^{122,123,124}Te, gives an impetus to study the s-process nucleosynthesis [17] in the mass region between A = 120 and A = 124 (where these three isotopes are situated)

In the synthesis of heavy elements the basic processes involved are the slow (s-) and rapid (r-) neutron capture processes and the proton (p-) capture process. This p-process synthesizes the neutron deficient isotopes of heavy elements. As the tellurium isotopes are produced in s-process nucleosynthesis only, 1% level of the tellurium isotopes ^{122,123,124}Te therefore can be satisfied by the classical model. Considering the available standard table of isotopic compositions and "local approximation", Kappeler *et al* [17] pointed out that the isotopic ratio ^{123}Te/^{124}Te agrees with the classical "local approximation" model as well as with the current p-process scenario. But de Leater [18] argues that constraints in estimation of the magnitude of the p-process contribution to ^{122}Te appears due to an error existing in the available Standard Table itself. Here Kappeler *et al* [17] also indicate that 1.8% excess yield in ^{122}Te abundance during s-process yield calculation may be due to p-process contribution and the magnitude of this excess yield is comparable with the magnitude of p-only isotopes ^{120}Te. They also speculate that small p-process contribution to ^{124}Te may have some effect on the ^{124}Te abundance Thus, accurate measurement of absolute isotopic abundance for tellurium in the mass range $120 \leq A \leq 126$ is very crucial in order to understand the validity of classical s-process as well as nucleosynthetic processes in this mass range.

2.2. r-process :

The rapid (r-) neutron capture process occurs in a high neutron density environment so that neutron captures are faster than beta decays. As a result, overall shapes of r-process abundances as well as the positions of the peaks in the abundance curve depend on the superposition of neutron densities. Laboratory experimental informations indicate that improved very accurate measurement of solar r-process abundances are essential for precise analysis of ther abundance distribution peaks in the $A \approx 80$ and $A \approx 130$ regions (see Figure 1). Not only that, neutron number densities and temperatures are very important to reproduce that solar r-process ratio because the validity of the waiting point approximation (WPA) depends on high temperature and neutron number densities of the gas while the abundance flow from each isotopic chain to the next depends on beta decay If one considers an $(n,\gamma) \Leftrightarrow (\gamma,n)$ equilibrium close to A = 80 and A = 130 peaks, then only one isotope with neutron magic numbers N = 50 or 80 has a substantial abundance Under all these above considerations it is evident that the origin of solar r-process abundance is from a freeze out abundance of an r-process with high neutron densities ($n_n \geq 10^{20}$ cm^{-3}) and temperatures ($T \geq 10^9$ K) excluding the scenario of explosive He burning [19]. In order to solve this problem Kappeler *et al* [17] suggested considering the global abundance pattern, *i.e.* assuming a global steady flow and using a freeze out temperature T_9 = 1.3, one can get information on the details of each peak with individual fit on the plot of local steady flow as a function of neutron number density (n_n). Figure 3 shows the global abundance curve as obtained by Kappeler *et al* [17] using the waiting point and steady flow approximation with temperature T = 1.3 × 10^9 K and neutron number density (n_n) = 7.6 × 10^{19} cm^{-3}. Various best fits for $A \approx 80$, 135 and 195 peaks with various neutron number densities are shown in Figures 3(b)–3(f). For $A \approx 80$ peak, Figure 3(a) and Figure 3(b) indicate the best fit for a neutron number density around n_n = 7.6 × 10^{19} cm^{-3} Below A = 77, no choice of n_n gives the best fit. It is seen from Figures 3(c) and 3(d) that two sets of half lives (due to superposition to two or more global steady flows and over production) are dominant at the $A \approx 130$ and $A \approx 195$ peaks. As a result, component-wise best fit for a single peak is not available. So, the steady flow approximation is valid in the region between neutron magic numbers and the lower part of each peak *i.e.* for short half lives, but not for longest half lives which require different n_n conditions for explaining each peak. As the beta decay rates are governed by the half lives ($T_{1/2}$) of very rich nuclei, Kratz *et al* [20,21] suggested that beta decayed neutron emission

should be considered for reproducing the solar system r-process abundances at least locally in the $A \approx 80$ and $A \approx 130$ peak regions (see Figures 3e and 3f).

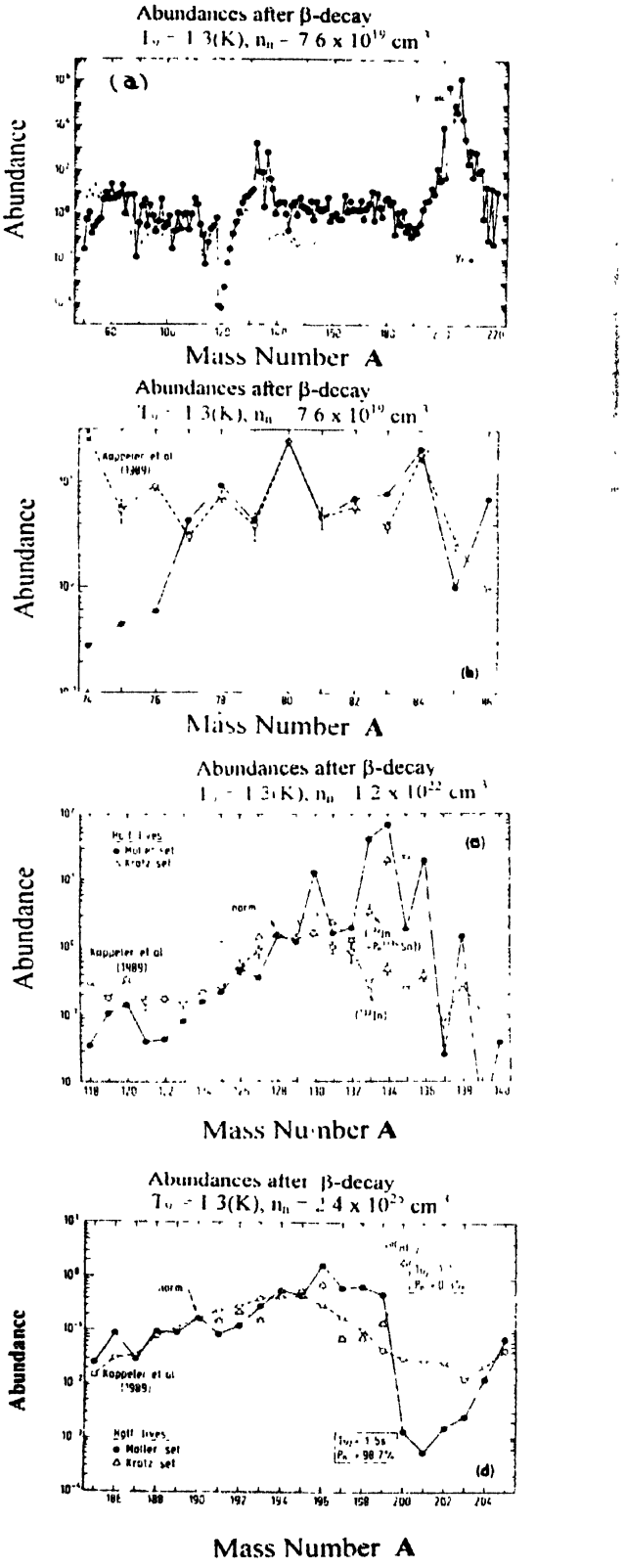

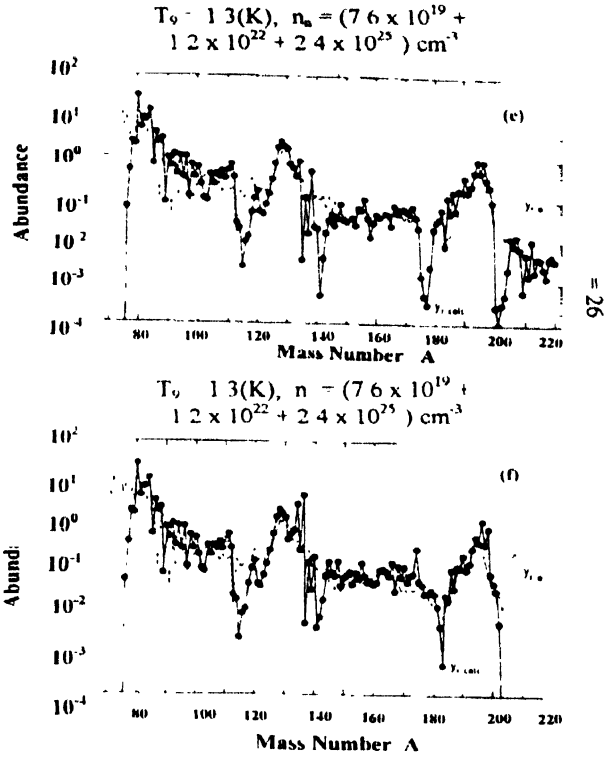

Figure 3. (a) Global abundance curve obtained by using the waiting point and steady flow approximation with T_9 1.3 (*i.e.* T 1.3 10^9 K) and a neutron number density n_n 7.6 10^{19} cm^{-3}. The dashed line indicates the solar r-process abundances. (b-d) Best fit for abundances around (i) $A \approx 80$ peak (ii) $A \approx 130$ region and (iii) A 195 region with temperature T_9 = 1.3 K and neutron number density n_n = 7.6 · 10^{19} cm^{-3}, 1.2 · 10^{22} cm^{-3}, and 2.4 10^{25} cm^{-3} respectively. The full points are 'Moller Set' data [23] which are improved version of data calculated from exclusively QRPA predictions [24] of half-lives $T_{1/2}$ and delayed neutron emission probabilities (P_n) of the progenitor isotopes in or close to the r-process path. Open triangles are 'Kratz Set' data [25] containing experimental values including first forbidden beta decays from the Gross theory. Open points are Kappeler set data [9]. Global r-abundance curve obtained from a super-position of three time-dependent calculations with the best fit n_n values for (e) the $A \approx 80$ peak (n_n = 7.6 · 10^{19} cm^{-3}), the peak $A \approx 130$ (n_n = 1.2 · 10^{22} cm^{-3}) and the $A \approx 195$ peak (n_n = 2.4 · 10^{25} cm^{-3}), and for (f) the $A \approx 80$ peak (n_n = 7.6 · 10^{19} cm^{-3}), A = 130 peak (n_n 1.2 × 10^{22} cm^{-3}) and the $A \approx 163$ sub peak (n_n = 2 · 10^{23} cm^{-3}) which improves the agreement with the solar abundances (from Refs. [19] and [26]).

The impact of neutron emission due to beta decay on the final shaping of isotopic abundances with observed r-process peaks and the parts of the (n_n - T_9) band which are responsible for different mass ranges of the solar r-process abundances is shown in Figure 4. This Figure clearly shows that the predictions of waiting point approximation and steady flow models in the areas around $A \approx 80$, $90 \leq A \leq 100$ and $A \approx 130$ are in good agreement with the r-process abundance features in the range $90 \leq A \leq 100$ occurring at T 1.0×10^9 K and $n_n = 10^{20}$ cm^{-3}. The solar r-process abundance which originated from freeze out abundances of an r-process, indicates (n,γ) ⇔ (γ,n) equilibrium with $n_n \geq 10^{20}$ cm^{-3} and $T > 10^9$ K. But the main difficulty appears in the production

of neutrons through (α,n) reactions which is insufficient in realistic stellar conditions [22]. Secondly, for the abundance

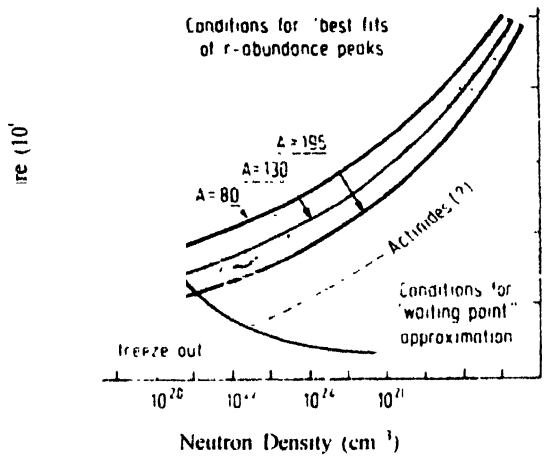

Figure 4. Neutron number densities and temperatures consistent with observed r-process peaks and measured beta-decay rates [29] Condition for validity of the classical waiting-point approximation found by Cameron *et al* [28] are also shown The temperature and densities produced in an r-process environment before freeze out is schematically indicated by thick arrow (from Ref [19]).

peak at $A \approx 195$, the best fit is obtained with $n_n \sim 3.0 \times 10^{22}$ cm^{-3} and $T \sim 1.2 \times 10^9$ K, *i.e.* the required neutron density is higher by two orders of magnitude. Thirdly, for the whole region between $A \approx 130$ and $A \approx 195$ with the above $n_n - T_9$ conditions, some local deficiency around $A \approx 142$ appears. For the nuclei beyond $A \approx 200$ there are may uncertainties in conditions which produce such r-process nuclei.

2.3. r-/s- *process controversy*

It is clearly understood from the above discussion that elements heavier than iron are mainly produced through two main neutron capture mechanisms – the slow (s-) process and rapid (r-) process which are distinguished by the magnitude of the availability of neutron flux. Contribution of these two processes to the synthesis of different isotopes is determined by the isotopic abundances of these elements in solar system material. Despite some difficulties in reproducing the detailed solar system abundances the sites for the operation of the r-process is more controversial than the sites of the s-process. Some controversies are discussed below :

(a) s-process abundances in AGB stars

In the asymptotic giant branch (AGB) stars, the s-process operates in the He shell. The s-process mechanisms in this case are identified as He shell flash or thermal pulses and the release of neutrons may occur prior to the thermal pulse at a time when the He shell is in a radiative condition rather than in the convective condition attained in the thermal pulse. The neutron exposure received by the material in the He-shell can be estimated from the abundances of the s-process elements in the AGB star's atmosphere. Here the s-process abundances of both the solar system and the stellar system will follow the same pattern only when the AGB stars

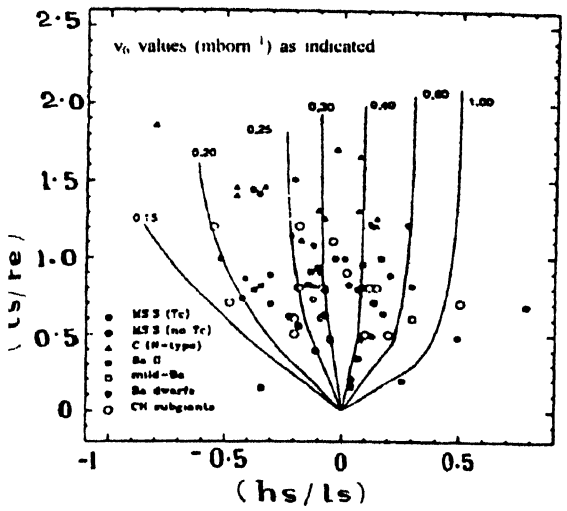

Figure 5. Comparison of theoretical predictions of surface abundances for different neutron exposures (solid lines) with observations of intrinsic and extrinsic AGB stars The abscissa represents the average logarithmic ratio of the abundances of the heavy s-elements Ba, La, Nd and Sm ("hs") to the lighter s-elements Sr, Y and Zr ("ls") The ordinate is the logarithmic enhancement in ls w r t Fe (After, Busso *et al* [37])

behave as primary sources for solar system's main s-process component and the neutron exposures of the stars follow an exponential distribution with $\tau_0 \approx 0.3$ for KT = 30 KeV, τ being the time integrated neutron flux. In general, this exponential distribution is considered as appropriate and the relative masses of s-processed material from the He-shell and unprocessed envelope material are determined by using the stellar abundance τ_0. But for cool AGB stars and for the warmer extrinsic (barium) stars the above method is very difficult to follow because the spectrum of the cool AGB stars is heavily blanketed by molecular bands. So, the search of rare lines of heavy elements under this condition ultimately puts a restriction on the selection of lines suitable for abundance analysis. Such a comparative analysis, studied by Smith and Lambert [27], is shown in Figure 5. In their analysis they consider heavy element abundances of M giants and intrinsic and extrinsic MS and S stars and compare the observed and predicted abundances of the total s-process enrichment or mixing fraction relative to neutron exposure. They found that the s-process (adding to MS/S stars) having $\tau_0 = 0.3 \pm 0.1$ gives a surprising result indicating a few stars having a τ_0 outside this range and a continuous spread in mixing fraction (Ms/Me) upto the value 0.004. They also observed that the location of extrinsic (without Tc) and intrinsic (with Tc) MS/S stars are indistinguishable provided τ_0 is not known for extrinsic AGB stars. However, using visible and near infra-red spectral parameters in investigating the s-process abundances for carbon stars it is also found that cool carbon stars seem to be more s-process enriched than the MS/S stars characterized by $\tau_0 \approx 0.2$ mb^{-1} while

barium giant stars indicate a higher τ_0 than the MS/S stars.

But analysis of the elemental abundances of intrinsic and extrinsic MS/S stars indicates that this s-process neutron exposures have a similarity with that experienced by solar system materials. This s-process also resolves the material of solar system composition in the Kr-Rb region into two components, namely the "main" component and "weak" component. The elements lighter than Kr are the dominant contributors for "weak" component while the dominant contributors of the "main" component are those elements heavier than Kr which are synthesized in the He-shell of low mass AGB stars and whose effects are seen in the MS/S and barium stars. In the case of massive stars, the r-process contribution to the solar abundances should be considered along with the main component because they are likely to be synthesized in the type II supernova and separation of the solar main component from the weak component and r-process component is very much essential [29]. In addition, the neutron density has some effect on the ^{85}Kr branch which causes a change in the abundance of Rb relative to the abundances of neighbouring elements. Figure 6 represents the recent result of Rb abundance

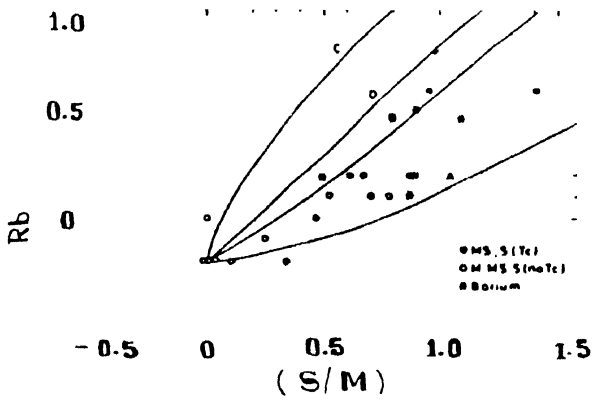

Figure 6. Observed and predicted correlation between Rubidium and s-process enrichments for M, MS and S stars and barium giants. Extrinsic and intrinsic MS and S stars are shown by open and filled circles, respectively. The predictions normalized to [Rb/M] = 0.2 and [S/M] = 0.0 correspond to enrichment with materials of different Rb abundances (a_{Rb}). For cases A, B and C the a_{Rb} = 1/5, 1 and 5 respectively. Case D indicates the expected relation if the added material has the solar abundances of Rb and the s-process elements (taken from Ref. [30]).

relative to the mean of [(Y/M) + (Zr/M)] abundance obtained by Lambert *et al* [30]. Considering five barium stars HR 774, ζ Cap, HD121447, HD178717 and 0 Vir they found that their obtained results for the M, MS and S stars are similar to the considered abundances relative to α-Tau while said abundances with respect to the M giants for the MS and S stars show different values. During the above analysis the following important features are found :

(i) Rb and s-process enrichments are well correlated in a similar fashion to the case of S and barium stars;

(ii) all M giants and α-Tau have apparently lower Rb abundances than that of the solar system;

(iii) s-process enrichments are interrelated with the sites of similar characteristics (*i.e.* neutron density and Rb/S where S is the mean of [(Y/M) + (Zr/M)] abundance).

The apparent Rb deficiency of M giants may be due to selection of s-process enriched stars only, systematic errors, *etc.* So, investigation of Rb abundance in stars other than the s-process enriched stars and associated standard stars, such as dwarfs, is necessary.

(b) Neutron density

The direction of s-process path along the valley of stability depends on neutron density. In low mass AGB star the abundance of Rb and Zr is sensitive to the neutron density. The branch point in the s-process at and beyond ^{85}Kr and the sensitivity of Rb abundance to neutron density are illustrated in Figure 7. A branch point in the s-process path appears because of the unstable ^{85}Kr and it controls the Rb

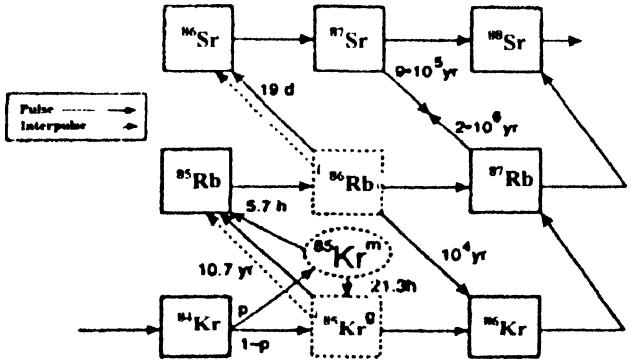

Figure 7. Synthesis of Kr, Rb and Sr isotopes during a thermal pulse (solid line) and in the interpulse phase (dash line) when the ^{85}Kr and ^{86}Rb which are built up decay. The population (P) of the isomeric state of ^{85}Kr is generated by neutron capture on ^{84}Kr (P = 0.52 ± 0.006 [28]). The time scales for ^{87}Rb and ^{87}Sr beta decay during pulse are significant for the synthesis while branching of ^{86}Rb to ^{86}Kr can be neglected (from Refs. [32] and [38]).

isotopic abundance during s-process operation. For example, in the case when neutron density $N(n)$ approaches to zero, the s-process follows a unique path along the valley of stability which will affect the Rb abundance. In this limit [$N(n) \rightarrow 0$] the dominant path is through ^{85}Rb, ^{86}Rb to ^{86}Sr and in the high density limit the path through ^{86}Kr to ^{87}Rb and ^{88}Sr is opened which runs in competition with the path through ^{85}Rb. The elemental abundance of Rb (relative to Sr and Y) is sensitive to the neutron density because of different (by a factor of about 10) neutron capture cross sections of two stable isotopes ^{85}Rb and ^{87}Rb. Here it is important to note that the Sr abundance is also sensitive to the ^{85}Kr branch and the variation of Rb/Sr ratio is more than

an order of magnitude between low and high density limits. However, Lambert *et al* [30] suggested that the Rb I line analysis will provide more accurate indication of neutron density than the Rb/Sr ratio. The Rb abundance analysis for neutron pulse *via* ^{85}Kr branch shows that the neutron density at the s-process sites does not exceed 10^8 cm $^{-3}$. Of course, this value may depend on the form adopted for the neutron pulse. But Beer and Macklin [31] show that pulses with a neutron peak density $N(n) \approx 10^8 - 10^9$ cm^{-3} are required to fit the observations.

Recent investigations [29] of ^{85}Kr branch indicate that

(a) at neutron density $N(n) \approx 10^7$ cm^{-3} the s-process path follows from ^{84}Kr to ^{85}Rb to ^{86}Sr without branching,

(b) $N(n) \approx 3 \times 10^9$ cm^{-3} is the critical density for the ^{86}Rb branch;

(c) at $N(n) \approx 10^9$ cm^{-3} the major part of the s-process path follows from ^{86}Kr, ^{87}Rb and ^{88}Sr with a second minor branch proceeding to ^{85}Rb and ^{86}Sr;

(d) for $N(n) \approx 3 \times 10^{10}$ cm^{-3} the direction of s-process path is from ^{86}Rb to ^{87}Rb and ^{88}Sr with a largely suppressed channel to ^{86}Sr.

Although the abundances of the dominant stable isotopes ^{85}Rb and ^{87}Rb in low and high neutron densities, sense the Rb elemental abundance, in real operation two complicated factors are to be considered because they affect the Rb abundance. The first one is the neutron capture on ^{84}Kr which leads not only to the long lived ($\tau_{1/2} \sim 10.7$ yrs) ground state of ^{85}Kr, but also to a short lived isomeric state ($\tau_{1/2} \sim$ 5.7 hrs). Experimentally determined branching ratio (P) will be 0.52 ± 0.08 at 25 KeV. According to Ward and coworkers [32,33], it is expected that this isomeric state will not come into thermal equilibrium with the ground state and this isomeric state will be treated as an effectively distinct nucleus for accurate modelling of the s-process during a thermal pulse. This causes two possible decay modes of the isomeric state - (i) beta-decay to ^{85}Rb with a probability of 80% and (ii) internal γ-transition to ^{85}Kr ground state with a probability of 20%. This means that the neutron density characterizing s-process route to ^{85}Rb remains open.

The second factor is the dependence of the final product on the temporal variation of neutron density, particularly, in realistic stellar condition such as bursts of neutrons released in the He-shell during a thermal pulse. In the case of final Rb abundance, for example, the yield of high Rb abundance *i.e.* ^{87}Rb primarily may be achieved at the peak of the neutron burst while restoration of low Rb abundance, takes place at the declining phase (*i.e.* the freeze out) of the burst. The way of neutron density declining controls the low abundance of Rb. In addition, the duration (Δt_n) of the neutron burst is also another crucial factor in determining the final Rb abundance. For example, short duration (less than the effective half-life of ^{85}Kr) of the neutron burst helps in the production of a little fresh ^{86}Kr and ^{87}Rb. Even in the short neutron burst with high neutron density less ^{87}Rb will be synthesized than in the case of a steady flow at some neutron density. Thus, for temperature $T \leq 3 \times 10^8$ K neutron capture rate, certain beta decay and electron capture rates are temperature dependent for ^{86}Rb and ^{87}Sr while the decay of ^{85}Kr is effectively constant.

Figure 8 (a and b) shows the aspects of the s-process path near Sr and Zr controlling the production of the stable isotopes ^{96}Zr. At the neutron densities that result in synthesis

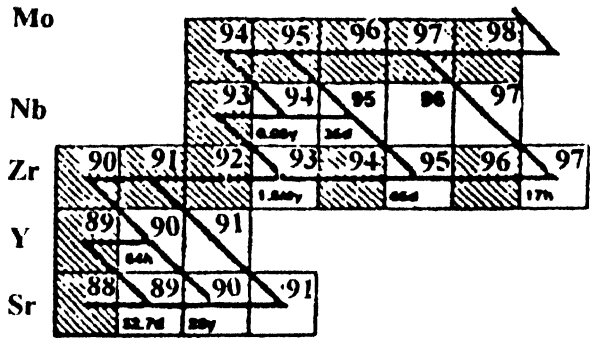

Figure 8. (a) s-process path from Sr to M_Q for neutron densities of 10^{10} cm^{-3} or less. Stable nuclei are indicated by striped box and unstable nuclei by open box. The half life of ^{94}Nb is quite temperature sensitive and the value for $T = 2 \times 10^8$ K is given. Major branches are given for neutron densities $N(n) \leq 10^{10}$ cm^{-3} (from Ref. [30]). (b) The main s-process flow through the Zr–Tc region of nuclei. Stable isotopes are indicated by cross-hatching (Ref. [38])

of ^{96}Zr, the major flow is from ^{89}Sr to unstable ^{90}Sr and then to ^{91}Zr by synthesizing a little ^{89}Y and ^{90}Zr. At low neutron density (*i.e.* less than a few times 10^8 cm^{-3}) the s-process produces the isotopes ^{90}Zr, ^{91}Zr, ^{92}Zr, and ^{94}Zr such that the isotopic abundances are roughly set by $\sigma(^{i}\text{Zr})N(^{i}\text{Zr}) \cong$ constant. As the neutron capture cross section of the stable isotope ^{96}Zr is the smallest of the sequence $^{90\text{-}96}$Zr, the ^{96}Zr isotope is produced at higher neutron densities than the critical density for the ^{95}Zr branch. The ^{93}Zr isotope, which like Tc measures the time elapsed since s-processing and is effectively stable at the s-process site, decays to ^{93}Nb. But as the Tc isotopes have shorter half lives than ^{93}Zr, the s-process path bypasses ^{93}Nb (which is only synthesized from the decay of ^{93}Zr) after the s-process has ceased. For intermediate mass AGB stars the s-process path at ^{85}Kr takes primarily the branch through ^{87}Rb and leads to a "high" Rb abundance with a non-solar isotopic ratio. The ratio of the Rb/Sr for different core masses (M_c) and peak neutron density $N(n)_{pk}$ are shown in Table 1.

Recent calculations [29,35] also indicate that

(a) earlier adopted neutron capture cross sections adopted by Malaney [34] differ by up to 30% from currently recommended values;

(b) the ratio Rb/Sr ≈ 0.05, obtained from either the solar system's relative abundances of Rb and Sr or the s-processed abundance ratio calculated from MS/S and classical barium stars, does not match the above predicted values.

Table 1. Rb/Sr ratio for different core masses

Peak neutron density $N(n)_{pk}$	Rb/Sr ratio	Core mass M_c	References
5×10^{9}–2×10^{12} cm^{-3}	≈1.0	1.36 $M_\odot$	Malaney [34]
	≈0.7	1.16 $M_\odot$	
	≈0.45	0.96 $M_\odot$	
2×10^{11}–3×10^{9} cm^{-3}	≈0.6	1.16 $M_\odot$	Beer and Macklin [31]
	≈0.2	0.6 $M_\odot$	
—	1.5–4.0	>1.6 $M_\odot$	Busso *et al* [36,37]

As a possible reason of this Rb/Sr discrepancy Beer and Macklin [31] suspected the profiles of neutron bursts having the same basic shape as the intermediate star bursts but of lower neutron density. Using the exponential distribution of neutron exposures with neutron density profiles they found Rb/Sr ≅ 0.07 for neutron peak densities $N(n)_{pk} \approx 10^{8}$–10^{9} cm^{-3} inferred from stellar observations. This value still remains lower than the Rb/Sr ratio observed in the barium giant stars. In order to solve this problem Beer and Macklin modified the profiles for the neutron bursts by proposing "Hot Bottom Burning Phase" model, *i.e.* inclusion of the effects of mass loss and of hydrogen burning at the base of the convective envelope in their earlier model for reducing the maximum temperature attending the thermal pulses. However, using the asymptotic limit $T \approx 3\times10^{8}$ K recent measurements show a high Rb/Sr ratio (≥ 1.5) because of the fact that the lower neutron exposure affects Sr more than Rb. More investigations in the s-processed materials produced at low neutron density as well as decay of the unstable nuclide ^{85}Kr rather than neutron capture in low mass AGB star only can provide the clues of this stellar Rb abundance conflict for barium giant stars and for other stars also.

3. An overview of the earlier problems

3.1. Star formation :

Star formation environment, where conversion of interstellar gas into stars takes place, plays an inportant role in understanding the physics of stellar nucleosynthesis. Theoretical calculations and observational evidences [39,40] suggest that stars form by contraction of interstellar clouds of gas and dust found in the galaxy, *i.e.* in the dense cores of 10^{4}–10^{6} $M_\odot$ giant molecular clouds, which contain a comparable amount of atomic hydrogen (HI). During star formation the basic process involves the gravitational collapse of molecular cloud fragments. Recent studies [41,42] of star formation regions indicate that

(i) most of the molecular gas (in the form of giant cloud complexes) have internal number densities ~10^{3} cm^{-3} and diameter ~100 pc;

(ii) the molecular and atomic surface densities (*i.e.* so called average gas surface densities) play a crucial role in disk average (*i.e.* averaged over the optical diameter of the disk) star formation rate, in particular on the average Hα disk surface brightness;

(iii) although the coupling between the star formation rate and molecular surface density is surprisingly weak, the star formation rate has a strong correlation with the HI surface density.

The correlation study [43] considers the cloud formation/destruction process as one of the important factors determining the star formation efficiency in the internal cloud process dominated star formation region. This gives the occurrence of the threshold at surface densities ~10^{21} H cm^{-2} in the active star formation region with a significant variation between galaxies. On the other hand, VLA observations show the appearence of large spatial variation in HI density in galaxies indicating the possibility of other threshold mechanisms in the cluster at critical densities near 10^{21} H cm^{-2}. Here the behaviour of molecular gas formation/gravitationally bound cloud formation as a crucial regulator of star formation is also another important factor. It is understood from numerical simulations and model calculations [44,45] that the star formation becomes more rapid than the observed one due to the influence of self gravity, gas cooling *etc*. However, still unknown areas are :

(a) the question whether molecular gas formation or gravitationally bound cloud formation controls the star formation;

(b) the portion of a molecular cloud collapsing to form a star;

(c) poor understanding of the mechanism of dominance of non-thermal motion over thermal motion.

These uncertainties in the protostar arise because of the missing link between the dense molecular cloud cores and embedded pre-main sequence stars.

3.2 Abundances :

Production of a considerable amount of neutrons in the s-process begins from helium burning phase and a part of this yield of neutrons is used to initiate neutron capture reactions in the next stage. In massive stars this chain continues till the formation of an Fe-core which finally goes through the supernova phase. In the supernova phase the s-process (slow) changes its direction to r-process (rapid) and various r-process mechanisms arise depending upon different locations within the supernova (*i.e* neutron density, time scale, *etc*). As the excess neutrons characterise the initial matter as well as raise the ratio of neutron to seed nuclei the exact neutron density in this stage is very much important and not only in that the large ratio of neutron to seed nuclei may finally stimulate the r-process. The investigations [44,45] of the behaviour of neutron number density and temperature during the time evolution of r-process phase of nucleosynthesis indicate that at the beginning of r-process the trajectories which contribute to the r-process abundance peak A ~130 or below produce fewer neutrons per seed nucleus (*i.e.* fewer heavy nuclei produced) while the

trajectories at the late stage produce a larger number of neutrons per seed nucleus giving a strong abundance peak at A – 195. Normalization of all the parameters in the calculation of above mentioned peaks with reference to the fixed abundance peak isotopes shows that all the r-process isotopes are within a normalized bound which is about 10 times the solar abundance. This value is in good agreement with the models calculated from the average of every supernova but poses a problem for supernova from low mass progenitor stars which are not efficient in producing the heavy r-process nuclei. This value also creates another problem in explaining the shift in the A = 95 peak by a couple of mass units and the over production of A = 180.

3.3. Helium burning :

Hydrogen exhaustion at the end of hydrogen burning in a star's main sequence phase leaves a helium core at the centre of the star and the contraction phase of the star then enables the helium core to activate helium burning through alpha capture process. It is believed that alpha capture process becomes active as soon as ^{12}C is formed which finally produces ^{13}C by mixing with hydrogen at high temperature through the reaction $^{12}C(p,\gamma)^{13}N(\beta^+,\nu_e)^{13}C$. Here, the reaction cross section of $^{12}C(p,\gamma)^{13}N$ plays an important role in understanding the role of ^{13}C as a neutron producer. The experimental study of the behaviour of $^{12}C(p,\gamma)^{13}N$ reaction in the excitation energy range 40–54 MeV shows that :

(A) no resonant decay of ^{13}N either at ground state or at excited state takes place but a coupling of single proton to the excited ^{12}C core in the excited states at 6.36, 7.38 and 9.00 MeV is indicated with an observed cross section of the order of 1.5–2.0 μb. This value is surprisingly large, being nearly half as big as the cross section for the direct transition;

(B) the observed values of surface $^{12}C/^{13}C$ ratio are in good agreement with the predicted values except for α Ori star and the star of mass below 3.0 $M_\odot$. The observed values of the ratio $^{12}C/^{13}C$ for α Ori star is extremely low which is not yet understood at all while for the stars with masses below 3 $M_\odot$ the observed values are so peculiar that these can not be explained only by the first dredge-up scenario;

(C) there is a good agreement between the observed and predicted values of oxygen isotopic ratio $^{16}O/^{18}O$ but in the region where ^{13}C is mostly produced, the oxygen isotope ^{18}O seems to survive destruction mainly by $^{18}O(p,\alpha)^{15}N$. In the red giant phase the first and second dredge up contribute a minor increase in the $^{16}O/^{18}O$ ratio while the third dredge up gives a huge increase in the $^{16}O/^{18}O$ ratio for the AGB stars of masses ≥ 5 $M_\odot$. This indicates the primary dependence of the ratio $^{16}O/^{18}O$ on the initial composition of the star, not on the star mass;

(D) there is a high destruction of ^{17}O by the raction $^{17}O(p,\gamma)^{18}F$ and $^{17}O(p,\alpha)^{14}N$ in the massive stars and the resulting surface ratio $^{16}O/^{17}O$ in a red giant phase is controlled by the maximum depth of the convective envelope of the star. The observed and predicted values of $^{16}O/^{17}O$ ratio are in good agreement for 2 $M_\odot$ stars but deviation arises for those stars having masses below and above this mass. For higher mass (>2 $M_\odot$) stars another problem is that the second and third dredge up significantly decrease the oxygen isotopic ratio $^{16}O/^{17}O$ in contrast with a huge increase in $^{16}O/^{18}O$.

3.4 Carbon burning .

$^{21}Ne(\alpha,n)^{24}Mg$, $^{22}Ne(\alpha,n)^{25}Mg$, $^{13}C(\alpha,n)^{16}O$ are the three controversial reactions during carbon burning phase. At temperature above 8×10^8 K $^{21}Ne(\alpha,n)^{24}Mg$ can be as efficient a neutron producer as $^{22}Ne(\alpha,n)^{25}Mg$ or $^{13}C(\alpha,n)^{16}O$ reaction at one point or another in this burning phase. As the shell C burning begins at very high temperature ($T_9 \sim 1$) with a high average neutron density ($\sim 10^{11}$ cm^{-3}), the external carbon shell burning affects the nuclear process in the carbon burning core and at the beginning of shell C burning the reaction rate of $^{12}C(\alpha,\gamma)^{16}O$ reaction plays a crucial role for calculating the evolution of convective mixing near the end of core He burning. Various resonances of the reaction ($^{12}C + ^{12}C$) and resonance like features near coulomb barrier at high energies also give another problem in this carbon burning phase. High neutron density also creates further problems in this phase, particularly, depletion of ^{63}Cu due to the strongly favourable situation of neutron capture by ^{63}Ni, over production at high neutron density. Theoretical calculations suggest that the weak component contributes only 30% to ^{64}Ni and s-process gives 30% contribution to the solar abundances of ^{63}Cu and ^{65}Cu. But study of average neutron density indicates that the average neutron density, mostly supplied by this-process, never exceeds 10^6 cm^{-3} in the core He burning in the stellar interior *i.e.* ^{63}Ni and ^{64}Ni are weakly produced. The exact reason of this is not yet known.

3.5 Oxygen burning :

At temperatures $> 8 \times 10^9$ K, oxygen shell burning in a massive star produces Si seeds in Si–Ca quasi equilibrium groups, while large electron capture in the late stage of this oxygen burning produces iron peak nuclei. A study of stellar oxygen abundances indicates a correlation between neutron captured elements and the strongly variable O and Na abundances (produced through neutron capture synthesis). Analysis of the observational oxygen OI triplet and other oxygen lines showed that the discrepancies in the O abundances and O/Fe ratio still exist between the presently observed values and the earlier observed and predicted values of them. LTE and non-LTE model calculations for

oxygen abundance using the oxygen triplet λ 7771-5 also show that discrepancy in O/Fe ratio still remains.

Investigation of the hydrodynamical behaviour of shell oxygen burning through numerical simulations shows that an abrupt change in the ^{16}O abundance occurs in the initial stage and a small fluctuation (~0.05 in nuclear fraction) in the ^{16}O abundance of the late stage. Moreover, a significant composition inhomogeneity also appears, because of incomplete mixing of nuclear fuel from the stable region towards the hotter region of the convective zone, which perturbs density, velocity, electron fraction *etc*. Creation of "Hot Spots" in this region also affects the flow of fuel. Mixing of unstable ^{56}Ni nuclei with the new decay products is a source of great trouble for accurate measurement of decay products in this region.

3.6 Supernova phase :

At the end of its nuclear fuel a massive star suffers a supernova phase. It is believed that r-process nucleosynthesis occurs in this supernova stage so that within a short time scale (~ 1 sec) transformation in the final abundances of the ejected mass takes place. So, if the r-process mainly occurs in that case the abundances of its products in the ejecta will be a function of initial stellar metallicity. This means that exact estimation of heavy element abundances produced through s- and r-processes before the explosion and heavy element abundances after the explosion (*i.e.* formation of dwarfs, neutron stars, *etc*) play an important role towards understanding the dynamics of supernova. Recent abundance analysis of neutron rich elements shows that element to iron ratio for the group of elements from Ba to Eu increases with the atomic number for the stars with ($-2 <$ Fe/H < -1), but is slightly deficient by a factor of ~0.1 dex in case of lighter elements (Ba, La, Ce *etc*) Even for most metal poor stars (with Fe/H < -2.5) large deficiency is also present for all these groups of elements with no clear evidence for a plateau at very low metallicities. The observed spread in the element to iron ratio for these elements is larger by a factor of 0.1 to 0.15 dex but the origin of scatter is not yet clear.

3.7. Neutron star phase :

At the final stage of evolution of a massive star, an iron core is formed at the centre of the star. According to the prompt explosion mechanism, this core collapses abruptly in such a manner that a "Core Bounce" appears due to this and within a very short time (few milliseconds) shock waves lose their entire kinetic energy for stalling inside the outer edge of the initial iron core. After a short time interval (prompt explosion), neutrinos stream out from the newly born neutron star. The neutron star's strong binding energy at this stage drives a powerful shock into the overlying stellar mantle causing a matter depleted region (known as "Hot Bubble") which separates the central remnant and the ejected stellar envelope. Latest investigations of the final r-process abundances indicate that the seed nuclei at $A < 90$ in the hot bubble are already synthesized by alpha process in contrast to the earlier calculations which show that the seed nuclei are confined to neutron rich, Fe group elements in a highly neutronized material at high temperature and high densities. This gives a discrepancy in the bulk r-process abundances of the heavy nuclei in this region i.e. neutrino driven nucleosynthesis in the hot bubble phase of supernova explosion and solar system abundances of r-process nuclei.

4. Recent developments

4.1.1 Star formation

Stars are born in the dense core of 10^4 to 10^6 $M_\odot$ giant molecular clouds and gravitational collapse of these molecular cores can occur through two distinct modes *viz*. Magnetic supercritical collapse (occurs when inward pull of gravity overwhelms the outward pressure of magnetic field in a given region where sufficient density of material accumulates, *i.e.* a mass scales of order 10^3 $M_\odot$) and Ambipolar diffusion (occurs more slowly through the magnetic field and coupling of electrons and ions to it). Recent millimeter and sub-millimeter wave length observations [46-49] indicate the tendency of massive stars to appear in clusters, indicating the possible involvement of interaction between the formation of massive stars and their cluster neighbors. In the pre-proto-stellar phase of star formation gravitationally bound fragments are formed in the molecular cloud and it leads to proto-stellar collapse through the progressive evolution of higher degrees of central condensation. Ciolek and Mouschovias [50] suggest that this evolution of a magnetically subcritical cloud core appears due to the progressive loss of magnetic support by ambipolar diffusion. The typically developed specific angular momenta (*i.e.* angular momentum per unit mass) of the stellar mass fragments in gravitationally bound collapsing cores are about 5 orders of magnitude larger than those of stars interacting through mutual tidal interaction between adjucent cores (or by other differential forcing). As a result, such rotating cores collapse into disks and accrete mass onto a central proto-star because of the dissipation of their angular momentum. Soon after the formation of an accreting central proto-star, it becomes fully convective and supports a rigid, co-rotating (*i.e.* with the star), roughly dipolar stellar field. In this phase, the estimation of gravitational star formation as well as formation of open clusters for massive stars is, thus, very much important as it is believed that most massive stars are formed from open clusters [51-53]. Figures 9 and 10 show the gravitational star formation and formation and formation of open clusters for massive stars, respectively, as obtained by Myers and Fuller [53] from the observations through 1.3 cm NH_3 line. Considering both the thermal and non-thermal components of the velocity dispersion in a core of radius r_{obs} associated with a star of mass M_* they divided

the time evolution into three ranges [see Figure 9(a)]. The resulting non-thermal motion at r_{obs} in the pre-stellar core

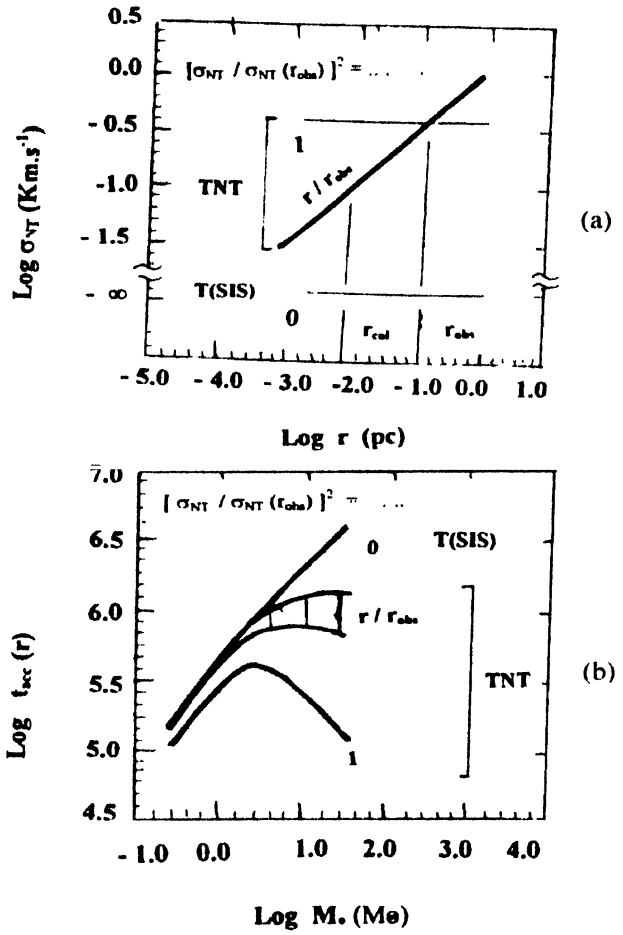

Figure 9. (a) Schematic diagram illustrating three assumptions about the radial structure of the non-thermal part of the velocity dispersion σ_{NT} in a prestellar core obtained by Myers and Fuller. For details see text. The mark TNT indicates the thermal and non-thermal motions observed in line widths are taking into account while T(SIS) indicates that non-thermal motions are neglected and thermal motions are assumed constant as in the singular isothermal sphere (from Ref. [53]). (b) Gravitational formation times t_{acc} for a core associated with a star of mass M_* to form a star or star-disk like system, as calculated by Myers and Fuller. See text for details (from Ref. [53])

is denoted by σ_{NT} and thermal motion which is assumed isothermal by σ_T.

Case I : When σ_{NT} $(r \leq r_{cool}) = \sigma_{NT}$ (r_{obs}).
In this case the observed value of the non-thermal velocity dispersion (with winds correction) is uniform for all $r \leq r_{obs}$, *i.e.* the non-thermal velocity dispersion inside radius r_{cool} is the same as that at the size scale r_{obs} sampled during NH_3 observation (Horizontal curve marked by 1).

Case II : when the non-thermal velocity dispersion is smaller than that observed at r_{obs} by a factor of $(r/r_{obs})^{1/2}$ (sloping curve marked by r/r_{obs}).

Case III : In this case the non-thermal motions are negligible and the accretion time depends on the thermal motions (horizontal curve marked by 0)

It is seen that σ_{NT} (r/r_{obs}) is uniform for cases 1 and 3 which is suitable for estimating the accretion time.

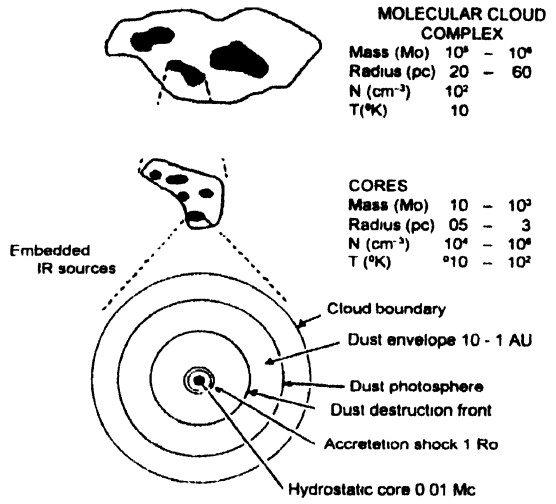

Figure 10. Schematic picture of star formation environment and proto-star model of Stahler *et al* [56] based on accretion paradigm of star formation. Molecular cloud data are from Blitz [54] (from Ref. [57])

Figure 9(b) shows the variation of gravitational formation times t_{acc} for a core, calculated by Myers and Fuller [53], against the associated star's mass M_*, to form a star or star-disk system. This formation time t_{acc} (*i.e.* the time required from the onset of spherical collapse to accrete a particular mass M_*) depends on the radial profile of the gas density within the radius r_{cool} which encloses M_*. In calculating t_{acc} they have considered the above three cases 1, 2 and 3 and found that the formation time is shorter time is shorter when non-thermal motions (cases 1 and 2) rather than the thermal motions are taken into account (case 3). This is because of the greater accretion rate (*i.e.* greater velocity dispersion). The range of formation times for the stars of masses 0.3, 1, 3, 10 and 30 $M_\odot$ is 1.1–1.5, 3–4, 4–8, 2–11 and 1–12 $\times 10^5$ yrs, respectively, *i.e.* all of the stars considered form within the range 1–12 $\times 10^5$ years for most massive stars. This range is significantly smaller than the range of stellar masses formed by molecular clouds. But for sufficiently massive stars the Kelvin Helmholtz time t_{K-H} for the stellar core to reach thermal equilibrium exceeds the gravitational infall time t_{acc}. Thus the systematic measurement of line width and map size in the densest parts of the core in the regions of massive star formation is essential for solving the above difficulties.

4.1.2. Accretion paradigm of star formation :

Figure 10 represents the modern picture of the accretion paradigm of star formation. To begin the main accretion

phase cluster cloud formation takes place. The main ideas regarding cluster forming cloud are that

(a) it consists of a spherically symmetric cloud component whose velocity dispersion varies with radius R as R^{-q};

(b) it is self-gravitating *i.e.* its density varies as R^{-2+4q};

(c) in this cloud smaller, spherical self-gravitating "Cores" are embedded whose total mass is small compared to the cloud mass;

(d) the pressure and density in the star forming part of the core are much greater in comparison to the corresponding pressure and density contributed by the cloud component;

(e) the variation of cloud pressure across r_{obs} is assumed negligibly small compared to the mean core pressure within r_{obs}.

It is believed that a cluster-forming cloud having a high pressure in its interior (also with a high pressure core) produces a more massive star than one with a low pressure core [55,56]. This indicates a tendency of more massive stars in a given range of stellar masses to form within a particular range of cloud radius and pressure. Figure 11 illustrates the distribution of stellar masses of the above mentioned model

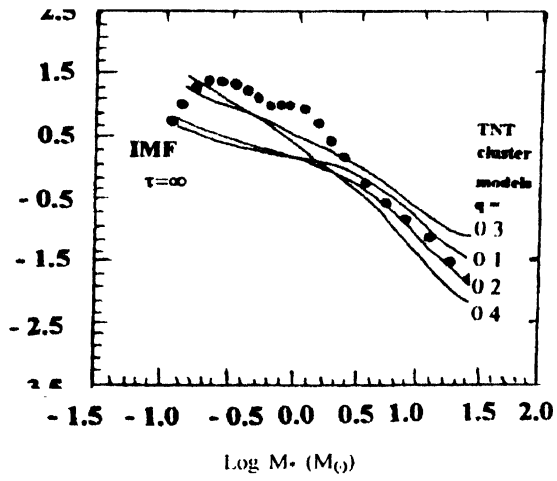

Figure 11. Variation of the distribution of the number of stars per unit logarithmic mass interval around $M_\bullet$ against $M_\bullet$. Solid lines – represent four models of a self-gravitating cluster cloud with embedded self-gravitating core. Curves are labelled according to the exponent q in the power law relation $\sigma \sim R^q$ between velocity dispersion σ and the radius R of the cluster cloud. Curves for $q = 0.1$ and 0.2 represent embedded core having constant mean density at the size scale traced by NH_3 line observations. While curves marked 0.3' and 0.4' represent core having mean density which decreases with increasing mass of their associated star. Filled circles represent the initial mass function (IMF) of Scalo [58] (This Figure is from Ref. [57])

by plotting $(\xi + C)$, the number of stars per logarithmic mass interval around $M_\bullet$, against $M_\bullet$ where

$$\xi = \frac{dM(M_\bullet)}{dM_\bullet} = \frac{dM_{\chi\lambda ou\delta}(> P_{\chi\lambda ou\delta})}{dP_{\chi\lambda ou\delta}} \cdot \frac{dP_{\chi\lambda ou\delta}}{dP_{\chi o\rho\iota}} \cdot \frac{dP_{\chi o\rho\iota}}{dM_\bullet}$$

or
$$\log\xi = C' + \frac{1+2q}{-1+4q}(\log\rho + 2\log\sigma) + \log\left(\frac{1}{\rho}\cdot\frac{d\rho}{dM_\bullet} + \frac{2}{\sigma}\cdot\frac{d\sigma}{dM_\bullet}\right)$$

with $C' \equiv \log(\varepsilon\, hyg^{-1})$,

ρ and σ are the mass density and the velocity dispersion of the core properties on the size scale traced by the NH_3 line during observation,

h = constant,

$\gamma = (1 + 2q)/(-2 + 4q)$,

$\frac{\varepsilon}{1+\varepsilon}$ the star formation efficiency,

g = a fixed multiple of pressure of cloud component observed at the core radius r_{obs} traced by NH_3 line observation.

The evaluation of the variation of ξ shows that the density profile is constant at 1×10^4 cm^{-3} for $M_\bullet \leq M_\odot$ and makes a smooth transition to 1.5×10^3 cm^{-3} at $M_\bullet = 30\ M_\odot$ and for each of these two density profiles ζ depends on the free parameter q, the exponent in the power law relation between velocity dispersion and radius in the cluster cloud. They have also choosen the value of "q" for each density profile such that the slope of log ζ *vs* log $M_\bullet$ closely matches that of the high mass part of the initial mass function (IMF) of Scalo [58], shown by filled circles in Figure 11. The values of "q" with no prime indicates the constant density profile while those with prime stand for the varying density profile. For more massive stars than 2–3 $M_\bullet$ this constant density range is 0.1 - 0.2 and variation density range is 0.3 – 0.4 which appears more realistic. The slope of IMF, following the observed relation between the core velocity dispersion and associated stellar mass, thus can account for the core of a self-gravitating cloud provided by the mean core density at the radius sampled by NH_3 lines. This means that the pressure distribution of cloud gas is the main factor which finally allows a sufficient number of cores to form in each interval of pressure. Because, if cluster clouds increase their internal pressure scale during their life time, their surviving cores and newly formed cores can then only have greater pressure w.r.t. the young stage of the cluster cloud, and their increased core pressure finally leads to the formation of more massive stars.

4.1.3. Core evolution :

The core formation takes place as soon as the cloud liberates enough gravitational potential energy to dissociate while the molecular hydrogen in the core and this central core continue to grow as long as material for accretion is available. During this main accretion phase, the outer layer of the dust envelope plays a key role in determining the observational characteristic of the proto-stellar cloud. The central accreting core is surrounded by a blanketing envelope of dust and the protostar becomes a prominent infrared source. But this protostar will not be in the visual part of the spectrum as long

as the above blanketing envelope dominates. When this surrounding envelope disperses the central core will be revealed as an optical object The accretion will then stop leading the core in the premain sequence phase (PMS)

Numerical studies of stellar birth line (*i.e.* the locus in the H–R diagram alongwith the star's first appearance as an optical object) suggest that the stellar birth line intersects the Zero Age Main Sequence (ZAMS) at a mass $M_{int} \approx 10\ M_\odot$ where the Kelvin-Helmholtz (K-H) contraction time scale is equal to the free fall time scale. Theoretical calculations indicate that for typical accretion rates of $10^{-5}\ M_\odot yr^{-1}$ and $10^{-4}\ M_\odot yr^{-1}$ this intersection will be at $M_{int} = 7.5\ M_\odot$ and $14.5\ M_\odot$ [59], respectively, while Beech and Mitalas [57] show that $M_{int} = 8.5\ M_\odot$ for an accretion rate of $10^{-5}\ M_\odot yr^{-1}$ If the contraction time scale is less than the free fall time scale then the protostar will reach the main sequence (MS). although the accretion process is still active For more massive star the Kelvin-Helmholtz time is shorter than the typical infall time and the star will appear in the optical region only during their MS evolution instead of PMS stage [56,59]

Figure 12 represents the accretion model of stellar evolution from $1\ M_\odot$ to $M_{int} = 8.5\ M_\odot$ obtained by Beech and

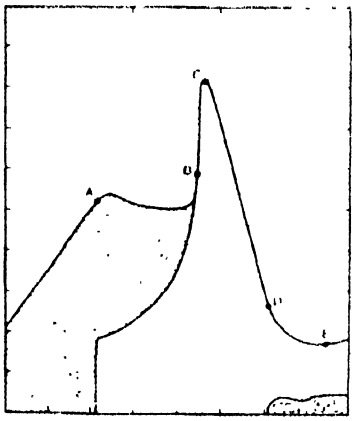

Figure 12. Variation of mass against radius for accretion model The upper curve gives the radius of the model while lower curve or radius of the convective zone. Scratched regions are convective

Point A	mass M	3.1 $M_\odot$, when a radiative barrier first appears.
Point B	mass M	5.4 $M_\odot$, when the interior becomes completely radiative.
Point C	mass M	5.6 $M_\odot$, when maximum radius is reached.
Point D	mass M	7.1 $M_\odot$, when convective core develops;
Point E	for M	8.5 $M_\odot$, when the accretion models join the canonical ZAMS (from Ref [57])

Mitalas [57]. They found four distinct evolutionary phases during the growth from $1\ M_\odot$ to $M_{int} = 8.5\ M_\odot$ with a time step of 2500 yrs and a mass increment of $0.025\ M_\odot$ during main accretion phase. Heavy dots represent for critical masses The fully convective phase of deuterium burning lasts upto the increasing mass $M = 3.1\ M_\odot$ (point A). Then shell burning phase begins and continues upto $M = 5.5\ M_\odot$ (point B). Point C indicates the mass $M = 5.6\ M_\odot$ at which the radius is maximum. A convective core appears at the end of the radiative interior phase which lasts upto the point D at which mass $M = 7.1\ M_\odot$ At point E, where the accretion sequence intersects the canonical ZAMS, the mass is $M = 8.5\ M_\odot$.

4.1.4. Fully convective phase :

According to the accretion paradigm the central temperature of massive stars is high enough for nuclear burning although the accretion process is still active. For fully convective phase the central temperature is $T \approx 2 \times 10^6$ K which grows slowly with mass and rises to $T \approx 2.5 \times 10^6$ K at $M = 3.0\ M_\odot$. During fully convective phase the radius varies linearly with the mass between 1.0 and $\approx 3.0\ M_\odot$ (point A in Figure 12) This fully convective phase ends when an off-center radiative region at a mass fraction of 0.25 appeared at model mass $M = 3.1\ M_\odot$. The appearence of radiative zone plays various important roles. First, it acts as a barrier and cuts off the supply of deuterium to the interior Second, due to this cutoff of deuterium supply, a local equilibrium state appears in the interior deuterium rapidly, which leads the interior to become radiative So, radiative interior exists for models more massive than $3.2\ M_\odot$. The mass fraction of the convective envelope becomes smaller and smaller with increased mass beyond $3.2\ M_\odot$ and the radiative energy transport becomes more active with increasing temperature between $3.2\ M_\odot$ and $5.4\ M_\odot$ (*i.e.* from Point A to Point B)

4.1.5. The radiative phase

When the model becomes fully radiative (at point B), its luminosity begins to increase rapidly. From Figure 12 it is seen that the radius is almost independent of mass between 3.2 and $5.4\ M_\odot$ (from point A to point B) and between 5.2 and $5.6\ M_\odot$ (from point B to point C) and a dramatic increase in radius against mass occurred. The maximum radius appeared at mass $M = 5.6\ M_\odot$ (point C) which indicates that a radiative interior has been established. At point B when it is fully radiative, there appears a rapid increase in luminosity. Figure 13 shows the variation of luminosity against mass for selected accretion models. It is seen that a steady increase in luminosity against increasing mass has occurred between points B and D where the luminosity of deuterium burning is small. However, the central and surface temperature of the accretion model increase dramatically because of increase in mass and luminosity with decrease in radius.

4.1.6. Central nuclear burning :

Figure 14 shows the evolution of the $D(p,\gamma)^3He$ reaction, the pp chain and CN cycle which are responsible for the central energy generation. Deuterium burning is the dominant energy

source for full convective models between 1.0 and 3.1 $M_\odot$. In this case the interior luminosity rises rapidly from the

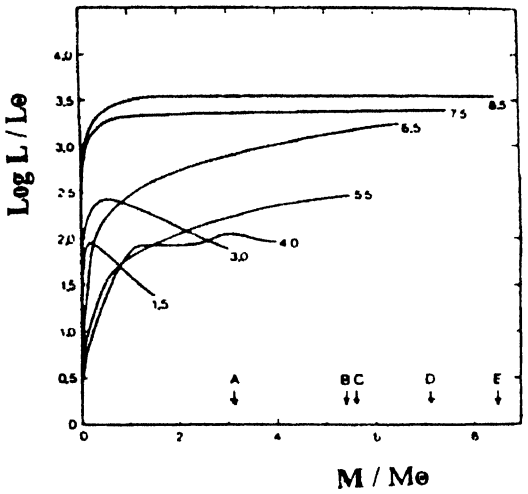

Figure 13. Luminosity as a function of mass for the accretion models labelled by their mass. Models of $M = 1.5\ M_\odot$ and $3.0\ M_\odot$ are fully convective. Model with $M = 4.0\ M_\odot$ shows the presence of dauterium burning shell at $M(r) = 3.0\ M_\odot$. Models with $5.5\ M_\odot$ and $M = 6.5\ M_\odot$ have rediative interiors whereas models with $M = 7.5\ M_\odot$ and $M = 8.5\ M_\odot$ have central convective cores. Points A, B, C, D and E are described in Figure 12. See text for details (from Ref. [57])

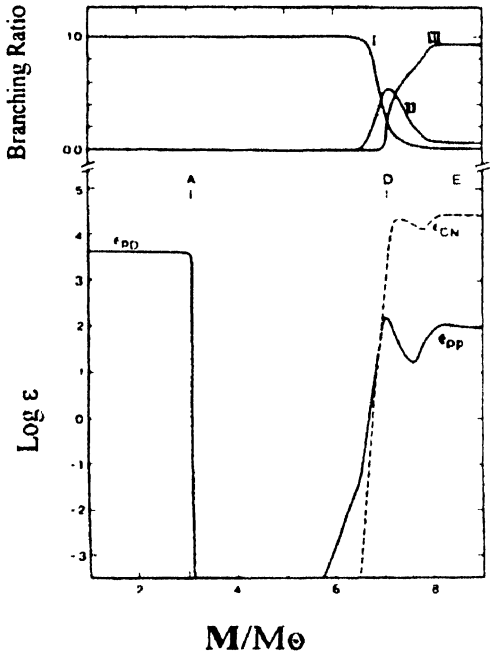

Figure 14. Central nuclear energy generation rates in ergs per gram per sec in the accretion model. The three branching ratios are shown in the upper panel. Points A, D, E are described in Figure 12. (from Ref. [57])

centre and attains the maximum at a mass fraction of order 0.2 and then falls gradually towards the surface. At $3.1\ M_\odot$ rapid depletion of the interior deuterium takes place after the appearance of the radiative barrier at this mass. The central convective process stops and as a result the nuclear energy generation rate drops dramatically but becomes significant again at a model mass $\approx 6.0\ M_\odot$ when the central temperature increases to $T \approx 6.8 \times 10^6$ K through the PP I chain reaction (marked by I). The energy generation through PP II chain reaction (marked by II) dominates at $7.1\ M_\odot$ with the central temperature at $T \approx 22.1 \times 10^6$ K while PP III chain dominates beyond $7.25\ M_\odot$ at a central temperature $\sim 25.4 \times 10^6$ K (case III). It is also seen from Figure 14 that the central convective core lasts around $7\ M_\odot$ and breaks up at $7.1\ M_\odot$ (point D). After that, the PP chain and CN cycle reactions proceed in a radiative core which grows rapidly in size with a mass fraction of 0.3 at $7.4\ M_\odot$ while the CN cycles maintain equilibrium at $8.3\ M_\odot$. Beyond $8.5\ M_\odot$ (point E) the radii maintain its increasing nature. The main problem in this case is that the $M_{\rm int}$ values vary in the range $7.5\ M_\odot$ to $14.3\ M_\odot$, according to theoretical calculations of Palla and Stahler [60,61], depending upon the increased accretion rate from 10^{-5} to 10^{-4} yr^{-1}. This indicates that although Beech and Mitalas have considered the value of $M_{\rm int} = 8.5\ M_\odot$ with an accretion rate $10^{-5}\ M_\odot$ yr^{-1}, a thorough investigation considering all the possible accretion rates is required in order to understand the core evolution.

4.2 Abundances

In analysing the features of heavy element abundances of the solar system we have mentioned earlier that the observed features are correlated with the position of neutron shell closures at $N = 50$, 82, 126 while analysis through splitting of the abundance peaks in the region $A = 80$–90, 130–140 and 190–210 indicates two scenarios with very distinct neutron fluxes (*i.e.* in quite different astrophysical environments), namely the s-process and r-process. Some pre-existing distributions of seed abundances, which are the only ones common to both, are exposed to neutron-irradiation, *i.e.* heavier elements are produced through subsequent neutron captures and beta decays. The comparison of the relative life time (τ) (defined as the mean time between subsequent neutron captures inversely proportional to the available number of neutrons and the reaction rate [62, 63]) for neutron capture (τ_n) and beta-decay (τ_β) clearly differentiate the s-process and r-process.

4.2.1 s-process and abundances

The condition $\tau_n \gg \tau_\beta$ in the s-process ensures that the neutron capture path will remain closed to the valley of beta-stability and the respective neutron capture cross section will therefore determine the resulting abundances. This means that :

(i) isotopes having small cross sections act as bottlenecks and produce large abundances;

(ii) isotopes with the s-process peak at magic numbers, will have small cross sections;

(iii) bottleneck isotopes, acting as neutron exposure monitor, determine the required mean s-process exposures;

(iv) a group of two, three or four radio-active isotopes are involved (such as ^{151}Sm, ^{152,154}Eu and ^{153}Gd) in the s-process branching;

(v) neutron density, temperature and electron density – all these can be estimated from the abundance pattern in such branching. This finally gives the scenario of three different s-process components for observed s-process abundances, namely :

(a) the Main s-process component – in this main s-process component a bulk of s-process isotopes between $90 \leq A \leq 204$ is produced and the exposure distribution $\rho(\tau)$ decreases smoothly with increasing neutron exposures (τ) [64,65];

(b) the Weak component – in this component the isotopic abundances below $\simeq 90$ are characterized by a smaller but continuous mean neutron exposures;

(c) the Strong component – this component is postulated in order to explain the very high ^{208}Pb abundance at the termination of s-process

4.2.1.1 Unpulsed s-process and single neutron source :

The above phenomenological approach to the s-process is based on the burning of only one neutron source for each of the components and final overproduction of exposure sensitive bottleneck nuclei at the magic neutron shell. In this s-process nucleosynthesis each isotope, from a potent seed like ^{56}Fe, can be formed and destroyed by neutron capture and beta decay following an unique synthesis path from ^{56}Fe to ^{209}Bi. As the s-process nucleosynthesis is essentially a function of three parameters, τ_0 (the total mean exposure), T_{max} (the temperature reached at the bottom of the convective He shell) and n_0 (the peak neutron density) a problem appears when the beta decay rate of a radio-nucleide is in competition with the neutron capture rat, because the beta-decay rate can be a strong function of temperature and also of electron density of the stellar environment [66]. Due to these, the s-process branching ultimately leads to the formation of other stable s-process isotopes in proportion to the above competition.

In order to solve this problem, first it is essential to know the s-process abundances responsible for the termination of s-process *i.e.* the main component and/or the strong component – whichever one causes the termination of the *s*-process. Secondly, the dependence of the s-process abundance (main part) on the exposure distribution *i.e.* whether the abundance is the result of one exposure (τ) or a superposition of exposures, also must be known :

$$\rho(\tau) = G\exp(-\tau/\tau_0) = (N_{tot,0}/\tau_0)\exp(-\tau/\tau_0),$$

$N_{tot,0}$ being the total seed abundance and τ_0 the average exposure.

Table 2. Capture areas of ^{138}Ba (energy range 1–200 keV) and ^{208}Pb (energy range 1–400 keV) resonances (compiled from Refs. Oberhummar *et al* [63], Corvi *et al* [69] and Beer *et al* [70]).

E_0 (keV)	Capture areas of ^{138}Ba (MeV)		Capture areas of ^{208}Pb (MeV)	
	GELINA	Mughabghab *et al* [71]	GELINA	Macklin *et al* [72]
00.64	4.91			
07.86	–	66.0 ± 2.0	—	–
29.19	60.0 ± 4.0	–	—	—
29.81	7.0 ± 2.0	—	—	—
30.80	–	90.0 ± 35.0	–	—
31.27	25.0 ± 3.0	–	—	—
40.26	–	69.0 ± 24.0	–	–
42.89	33.0 ± 4.0	–	–	—
43.34	—	–	26.5 ± 0.8	30.5 ± 3.2
43.74	32.0 ± 4.0	–	—	–
47.33		—	38.5 ± 1.2	38.0 ± 4.3
47.42	9.0 ± 3.0	–	—	–
47.53	64.0 ± 6.0	–	—	—
0.30	–	28.0 ± 14.0	—	—
68.20	66.0 ± 8.0	–	—	—
69.01		120.0 ± 51	—	–
69.29	16.0 ± 7.0	–	–	—
71.21	—		24.8 ± 4.0	70.0 ± 30.0
72.52	16.0 ± 6.0	–		—
73.02	62.0 ± 8.0	—	–	—
77.77	65.0 ± 9.0	—	–	—
77.85	–	—	250.0 ± 60.0	1076.0 ± 41.0
87.58	—	—	15.2 ± 6.0	< 25.0
87.38	32.0 ± 7.0			–
115.67	40.0 ± 11			—
116.73	–	90.0 ± 42.0	–	—
116.78	—	—	55.0 ± 20.0	276.0 ± 30.0
117.12	127.20		–	–
129.87	83.0 ± 34.0	48.0 ± 30.0	–	–
130.25	–	–	302.0 ± 12.0	374.0 ± 22.0
132.13	47.0 ± 11.0	–	–	—
151.73	151.0 ± 60.0	—	—	—
152.52	110.0 ± 20.0		–	–
153.31	—	—	53.2 ± 9.0	—
154.87	51.0 ± 16.0			—
169.39	137.0 ± 22.0	–	—	—
169.48	–		147.0 ± 6.0	170.0 ± 26.0
192.35	69.0 ± 19.0	–	—	—
193.69	—	—	277.0 ± 10.0	414.0 ± 29.0
194.27	39.0 ± 32.0	—	—	—
194.58	56.0 ± 31		–	–
199.80	35.0 ± 16	–	—	—
350.43	—	–	319.0 ± 34.0	—
359.14	–	—	253.0 ± 44.0	276.0 ± 14.0

4.2.1.2. Pulsed s-process and two neutron sources :

Pulsed neutron flux nucleosynthesis [66] was considered in order to overcome the deficiencies in the s-process models to explain the source of overproduction at the exposure sensitive bottleneck nuclei with magic neutron shell. As the overproduction indicates the unreliability of the stellar capture rates of these nuclei the model of combined burning of two neutron sources [67,68] was incorporated to understand the influence of newly determined stellar reaction rates of important isotopes on the s-process abundance distribution. As the s-process nucleosynthesis beyond ^{56}Fe is controlled by the small cross sections at the magic shells 50, 82 and 126, the synthesis of the main component can be monitored by ^{138}Ba and next double magic ^{208}Pb. The capture areas of ^{138}Ba in the energy range 1–200 keV and of ^{208}Pb in the energy range of 1–400 keV are shown in Table 3 [obtained from the measurement performed at GELINA (Geel Electron Linear Accelerator)]. Among the observed 12 resonances at E_0 (keV) = 43.34, 47.33, 71.21, 77.85, 86.58, 116.78, 130.25, 153.31, 169.48, 193.69, 350.43 and 359.14, respectively, the first 11 resonances were the previously observed and the new one is at 359.14 keV. In fitting the values of neutron width calculated from the above, to the earlier *R*-matrix fit of total and differential elastic scattering data of Horen *et al* [73] a discrepancy arises (because of non-availability of transmission data) in the correction for prompt background from resonance scattering. In the GELINA experiment no new resonances were observed but the strength of the resonances was found to be much lower than that previously reported in the ORELA experiment [74]. It turns out that direct capture is significant and sensitive enough to provide the correct total cross section at stellar temperature.

Table 3. MAC cross section (σ) of ^{138}Ba and ^{208}Pb as a function of stellar temperature kT

kT	σ (mbarn) for ^{138}Ba		σ (mbarn) of ^{208}Pb		
(keV)	GELINA Expt	ORELA Expt	Compound capture	Direct capture [75]	Total capture
5	13.57±0.47	5.78±1.19	0.0015±0.0001	0.056±0.001	0.058±0.011
7	10.43±0.38	—	—	—	—
8	—	—	0.018±0.001	0.070±0.014	0.088±0.014
10	7.99±0.31	5.25±0.08	0.039±0.003	0.079±0.016	0.118±0.016
12	7.01±0.29	5.12±1.04	0.063±0.005	0.086±0.017	0.149±0.018
15	6.03±0.26	4.89±1.00	0.102±0.009	0.096±0.019	0.198±0.021
17	5.56±0.25	—	0.126±0.012	0.102±0.020	0.228±0.023
20	5.04±0.23	4.57±0.94	0.151±0.017	0.111±0.022	0.268±0.028
25	4.46±0.21	4.23±0.87	0.196±0.023	0.124±0.025	0.320±0.034
30	4.07±0.20	3.90±0.80	0.221±0.027	0.135±0.027	0.356±0.038
35	3.78±0.19	3.60±0.74	0.235±0.029	0.145±0.029	0.380±0.041
40	3.55±0.18	3.33±0.68	0.241±0.029	0.153±0.031	0.394±0.042
45	—	—	0.243±0.025	0.162±0.032	0.405±0.041
50	3.20±0.17	2.90±0.59	0.241±0.028	0.169±0.034	0.410±0.044
60	2.94±0.18	2.59±0.53	0.231±0.026	0.180±0.036	0.411±0.044
70	2.73±0.19	—	0.216±0.023	0.189±0.038	0.405±0.044
80	2.56±0.21	—	0.201±0.021	0.194±0.039	0.395±0.044
90	—	—	0.186±0.015	0.195±0.039	0.381±0.042
100	2.27±0.26	—	0.171±0.017	0.195±0.039	0.366±0.043

Compiled from References [63, 70, 75]

To attack this problem the resonant Maxwellian Averaged Capture (MAC) cross section (*i.e.* compound capture) is required which can be calculated from Table 1 using the Breit-Wigner formalism. But it is expected that the nucleosynthesis of ^{138}Ba and ^{208}Pb are strongly temperature dependent, *i.e.* a significant change is expected in the s-process nucleosynthesis of these two isotopes. Recent MAC cross sections of ^{138}Ba and ^{208}Pb are presented in Table 3. It is found from Table 3 that the obtained total MAC cross section (*i.e.* the sum of the resonant part determined from experiment and the non-resonant part from theory) 0.356 ± 0.038 mbarn is in excellent agreement with the value (*i.e.* 0.36 ± 0.03) obtained from the activation experiment [76]

4.2.1.3. s-process abundance distribution and model calculation :

The Double Pulse (DP) model (the pulse combines burning of two neutron sources) gives more consistent result than the Single Pulse (SP) s-process. The natural consequence of this double pulse model is the He shell burning where two powerful neutron generating reactions, namely ^{13}C(α,n) and ^{22}Ne(α,n), exist. Figures 15a,b show the recent results of the

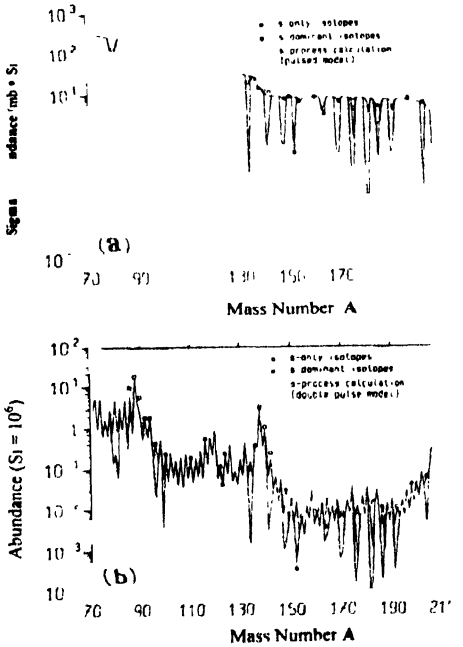

Figure 15(a) Main s-process calculation Single Pulsed model as obtained by Beer *et al* [70] considering the s- only isotope adjustment and MAC cross section times s-abundance *vs* mass number for only one temperature kT = 27.1 keV (b)Main s-process calculation considering the double pulse model with s-process temperature of kT = 12 and 28 keV (obtained from Beer *et al* [70])

main component of s-process. It is seen from the above s-process abundance distribution that the capture cross sections of the odd A isotopes are larger than the capture cross sections of the even A isotopes. The abundances of the bottleneck isotopes ^{88}Sr, ^{120}Sn, ^{138}Ba and ^{208}Pb reach peak values at the magic shells 50, 82 and 126 showing a dependence on the average neutron exposure. It is also seen that at magic neutron shell 50 the s-process is more siphoned than that at the magic shells 82 and 126. In the Kr–Sr region and Pb–Bi region this Single Pulsed (SP) and Double Pulsed (DP) models show their own significant role towards the termination of s-process nucleosynthesis. For example, using the DP model the abundance pattern in the Kr- Sr branching, originated from the ^{85}Kr branching, can be well described by the neutron density associated with the first pulse. The abundances of Pb–Bi branching are strongly influenced by the ^{208}Pb bottleneck and MAC cross section and using SP model a large deviation is observed among the s- only isotopes of the solar abundances and of ^{136}Ba. The overabundance of ^{136}Ba creates a new problem in the s-process calculation indicating a sensitive dependence of the s-process on the stellar parameters of the model [77,78] and secondly, the existence of succeeding isotopic chains of unstable nuclei in the ^{85}Kr branching [79] *i.e.* $^{84-86}$Kr, $^{86\ 88}$Rb and $^{86\ 88}$Sr. As the s-process branchings are characterized by a set of two or three succeeding isotopic chains having both unstable and stable nuclei, the theoretically calculated values of neutron capture of unstable branching isotopes are very much essential for s-process analysis. In Table 4 we have modelled the s-process synthesis using the various available s-process parameters.

Table 4. Parameterized s-process model

Astrophysical parameters	Values				References
	Burning of one neutron source (SP)		Burning of two neutron source (DP)		
	Main	Strong	Main	Strong	
Fraction of solar seed f_{seed}	4.72×10^{-4}	1.066×10^{-6}	5.543×10^{-4}	1.017×10^{-6}	[70]
Average exposure τ_0 (mbarn^{-1})	0.296	8.0	0.00340	-	[70]
Exposure per pulse $\Delta\tau$ (mbarn^{-1})	0.0159	--	0.0198	--	[70]
Neutron density n_n (cm^{-3})	3.2×10^{8}	—	5.0×10^{8}	- -	[70]
Mass density	$(4.1\pm0.6)10^{8}$	--	-	—	[80,84]
ρ, (g cm^{-3})	$(6.5\pm3.5)10^{8}$	—	—	--	[82,84]
Temperature (K)	3.14×10^{8}	—	3.25×10^{8}	—	[70,84]
			$(3.5\pm0.4)10^{8}$		[81,84]
			$(1.7\pm0.3)10^{8}$	--	[83,84]
Overlap factor	0.948	-	0.50	-	[70]
Isotopic abundances N(Si = 10^{6})					
^{86}Sr	1.991	0.001	1.945	0.001	[70]
^{86}Kr	6.550	0.009	5.100	0.008	
^{87}Sr	1.470	0.001	1.246	0.001	
^{87}Rb	1.418	0.002	0.483	0.001	
^{88}Sr	18.519	0.023	17.853	0.013	
^{116}Sn	0.428	0.001	0.442	0.0001	
^{136}Ba	0.417	0.002	0.382	0.001	
^{138}Ba	3.424	0.030	3.233	0.015	
^{140}Ce	0.924	0.011	0.977	0.006	
^{142}Nd	0.183	0.002	0.166	0.001	
^{198}Hg	0.035	0.0007	0.032	0.0003	
^{204}Pb	0.058	0.001	0.058	0.001	
^{206}Pb	0.306	0.027	0.347	0.010	
^{207}Pb	0.345	0.042	0.413	0.020	
^{208}Pb	0.834	0.816	0.633	1.042	
^{209}Bi	0.041	0.076	0.004	0.008	

Depending upon the physical conditions at the stellar sites, nearly 15 to 20 significant branchings occur along the s-process path [84]. The analysis of different branchings, which are not temperature dependent, can be used for calculating neutron density while s-process temperatures can be estimated from other branchings. But the physics of s-process can be well understood only from the stellar models. As the models are still plagued by a number of open questions, more investigations, both theoretically and experimentally (*i.e* laboratory studies) only can help us to have full understanding of the s-process nucleosynthesis.

4.2.2 Recent r-*process*

During our earlier discussion we mentioned various scenarios for the course of r-process but the details of the mechanism for the creation of conditions for the r-process are still unclear. Even the details of element formation in the r-process are not yet fully known. Recent solar system elemental abundance fractions attributed to the r-process are shown in Figure 16. All the stable neutron capture elements in the range $31 \le Z \le 83$ alongwith the important unstable

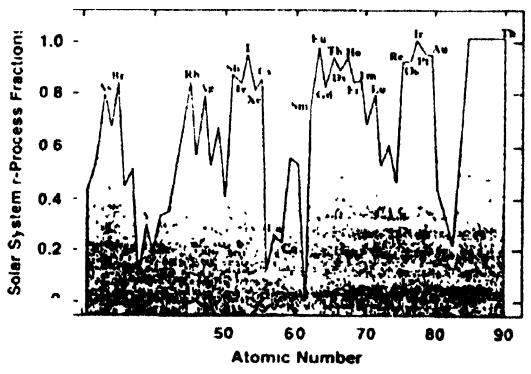

Figure 16. Fraction of neutron capture solar system element abundances attributed to the r-process as a function of atomic number as obtained by Sneden *et al* [85] and Cowan and Burris [86] by considering r- and s-process solar system isotopic fractions (Kappeler *et al* [17]) with solar system elemental abundances (Anders and Grevesse [13], Grevesse *et al* [13]) This Figure is from Ref [84]

element Th ($z = 90$), produced in the r-process, are also seen. Theoretically, 24 r-process elements have been identified but only a few of them are observable in stars. On the otherhand, several r-process elements such as As, Br, Te, I, Xe, Cs, Re have not yet been detected in the solar spectrum whereas several other r-process elements such as Ag, Lu, Os, Ir, Pt, *etc* are so crowded in the UV spectral region ($\lambda < 3500$ Å) that it is very difficult to detect them.

The main problem is still with the solar tin abundance (see Figures 17a,b) in which an inconsistency appears between the solar tin abundance obtained from meteorites

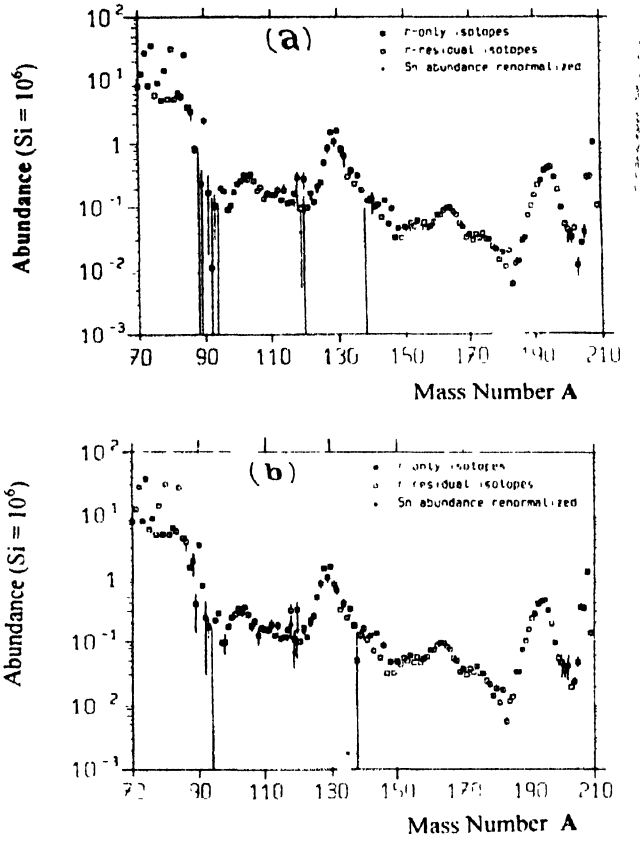

Figure 17. r-process residuals (No-N) of the DP s-process model Note that the abundances on the iron slope are not corrected for the weak s-process component (for $A < 85$ the correction is significant) and the abundances of $^{206\text{-}208}$Pb and ^{208}Bi are not corrected for the strong s-process component, the latter r-abundances are the sum of all transbismuth r-abundances The nuclei $^{206\text{-}208}$Pb contain in addition abundance from the ^{235,238}U and ^{232}Th decay The r-process residuals with a renormalized solar tin abundance are shown as well (a) $KT = 27$ keV and (b) temperatures $KT = 12$ and 28 keV (Figure is from Ref [70])

and from the s-process calculations through neutron capture measurement of the s- only ^{116}Sn isotopes and its associate isotopes [84–86]. This inconsistency also indicates a lower value, obtained from the meteorites, by 23% in order to fit the s- only isotope ^{116}Sn value in the σN curve while the r-process isotopic abundances of $^{115\ 118,120}$Sn are well in agreement with the r-abundance distribution. Recent analysis (Figures 17a,b) of tin isotopes with a renormalized solar tin indicates a possible reduction of 21% and 17% in the SP and DP models, respectively [70].

4.2.2 1. High Entropy Bubble – a new site of r-*process* :

In the above we saw that the r-process site is not clearly identified satisfying the basic requirements for the r-process *i.e.* neutron number densities $n_n > 10^{20}$ cm^{-3}, temperature around 10^9 K lasting for of the order of 1 second and the abundance ratio of neutrons over seed nucleus of $1 < Y_n/Y_{seed} < 180$ [63]. In particular, the r-process requires a sufficient supply of neutrons (*i.e.* 180 per seed nucleus to start with at $A \sim 60$) to synthesize the heaviest element at $A \approx 240$. The duration of r-process is very short (~seconds) and large neutron flux requirement within a short time scale suggests an astrophysical explosive origin of the r-process. Recently it has been suggested that the most favourable site for such an environment is the "High Entropy Bubble" of exploding type II supernovae [87-89].

At the end of Si burning, the iron core of a typical massive star will collapse when it exceeds the Chandrasekhar mass limit. But degeneracy formation in the nucleon gas helps the core to become stable again at nuclear density. The core will bounce back creating a shock wave which will run through the outer layers of the collapsed star. Due to this the shock heated material of the core becomes to much heated (4 7 MeV per nucleon) that photo-disintegration takes place among the iron nuclei produced earlier. This process will eventually halt the shock front and a "hot bubble" formation is suggested [90] which expands off the protoneutron star during a core collapse supernova. The formation of neutron star takes place with a release of gravitational binding energy in the form of neutrinos. Although these neutrinos are weakly interacting with matter, the deposition of considerable amount of neutrinos *via* neutrino captures on neutrons and protons may reheat the outer layer that accelerates the shock waves which ultimately help to explode the star. This heating and expansion thus creates a zone with low density and high temperature behind the shock front, the so called "High Entropy Bubble".

4.2.2.2 Nucleosynthesis in the high entropy bubble :

Due to high temperature the photo-disintegration process will become active and destroy the nuclei upto iron previously produced. At a temperature of about 10^{10} K the nuclei will be dismantled into their consituents, *i.e.* protons and neutrons. Because of expansion and cooling of this nucleon soup, almost all the protons would be locked into α particles and then α-processes will take place to burn alpha particles into the seed nuclei with A close to 100 [91]. In other words, during subsequent cooling of the nuclear soup the recombination takes place first to α particles through the reaction $3\alpha \rightarrow {}^{12}C$; then by r-process through the capture of excess neutrons on these seed nuclei : $\alpha + \alpha + n \rightarrow {}^{9}Be$, followed by $^{9}Be(\alpha,n)^{12}C$ and then to heavier nuclei. As a

result, a quite different r-process abundance distribution will be produced in the α-rich freeze-out depending upon the exact temperature, densities and the neutron excess w.r.t. the nuclear statistical equilibrium found in the late evolution phases of massive stars [91,92]. As the temperature and density drop quickly in the adiabatically expanding high entropy bubble the recombination of alpha particles into heavy nuclei leaves a high Y_n/Y_{seed} and sufficient neutrons for an r-process. However, various anomalies still remain in this adhoc r-process such as (a) overabundance of two heaviest stable isotopes ^{134,136}Xe and higher mixing ratio [93], (b) thorium loss (^{235}Th) [94]; (c) non-essentiality of "high entropy" scenario for successful production of A 195 r-process peak [95]; (d) the dependence of the nucleosynthesis process on the expansion and cooling rate as well as on the rates of alpha particle and neutron recombination processes; (e) exact role of the reaction ^{4}He(αn,γ)^{9}Be for initiating the a-process [96], *etc.*

This r-process nucleosynthesis can be affected by neutrino reactions with neutron rich heavy nuclei during the r-process and later on. A quantitative consideration of the competition between β-decay and charged current neutrino reactions in the context of hot entropy bubble dynamics is essential for understanding the realistic role of neutrinos in the r-process.

4.3 Helium burning :

In the helium burning phase, the heavier nuclei produced through neutron capture s-process, are usually divided into two categories, namely, a weak component (for $60 \leq A \leq 90$) and the main component ($90 \leq A \leq 205$). According to Prantzos *et al* [97] the s-process occurs efficiently in massive stars during core helium burning and produces the weak component of the s-process elements. Figure 18 shows the growth of the convective core of mass 8 $M_\odot$ (initial stellar mass = 25 $M_\odot$) where s-process nucleosynthesis occurs effectively. Convection starts at stage 50 from the centre and ends at stage 150 (*i.e.* the interval is 7.67×10^5 yr). From this figure it is also seen that when the size of the convective core reaches a maximum of 5.66 $M_\odot$ it suddenly disappears due to helium exhaustion. Table 5 represents the maximum size of convective cores for different massive stars while Figure 19 shows the neutron densities at the centre of different helium cores which is a function of helium mass fraction. It is clearly seen that the efficiency of the neutron capture is different for different massive stars.

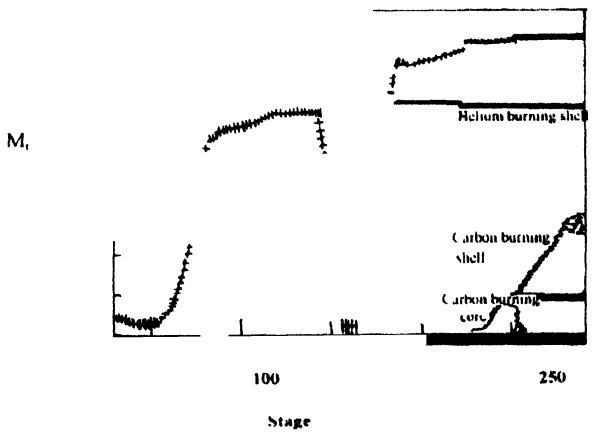

Figure 18. Growth and reduction of the convective core for 8 $M_\odot$ where the s-process nucleosynthesis occurs. Convective burning layers are shown for helium core burning, helium shell burning, carbon core burning and carbon shell burning (This Figure is from Ref. [100])

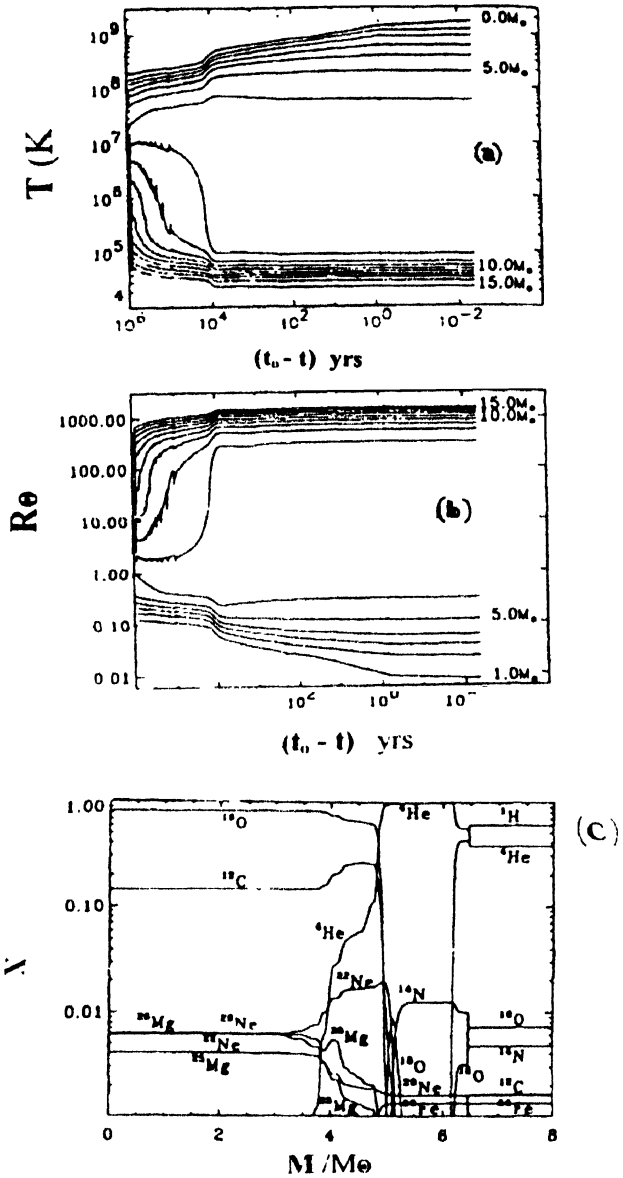

Figure 19. (a) Temperature- and (b) Radius-wise evolution of several layers of 20 $M_\odot$ star, during the advanced evolutionary phases of He, C and Ne burning as per Aubert *et al* [110]. Time is measured backward from the last point (central Ne exhaustion). Layers are separated by 1 $M_\odot$. Vertical dotted lines indicate ignition of carbon and neon in the centre. (c) Chemical profiles of the inner 8 $M_\odot$ of the 20 $M_\odot$ star at central He-exhaustion. The species are with mass fraction $X > 10^{-3}$ (from Ref. [110])

Table 5. Initial stellar mass, mass of He core, maximum size of convective core in $M_\odot$, mass fraction of ^{12}C and ^{16}O for two reaction rates (a) CFHZ 85 [98] and (b) CF 88 [99] (Hashimoto [100])

$M_{ini}/M_\odot$	$M_\alpha/M_\odot$	$M_{cc}/M_\odot$	X ^{12}C	X ^{16}O	$^{12}C(\alpha,\gamma)^{16}O$
9.0	2.5	0.96	0.289	0.692	(a)
			0.525	0.456	(b)
11.0	2.8	1.22	0.288	0.693	(a)
12.0	3.0	1.37	0.292	0.689	(a)
		1.38	0.452	0.529	(b)
12.5	3.2	1.55	0.288	0.689	(a)
13.0	3.3	1.62	0.245	0.735	(a)
		1.56	0.459	0.521	(b)
15.0	4.0	2.02	0.236	0.744	(a)
		1.98	0.488	0.492	(b)
18.0	5.0	2.86	0.225	0.755	(a)
		2.82	0.468	0.512	(b)
20.0	6.0	3.76	0.217	0.763	(a)
			0.449	0.530	(b)
25.0	8.0	5.66	0.186	0.793	(a)
			0.422	0.555	(b)
30.0	10.0	7.49	0.167	0.807	(a)
		7.50	0.403	0.572	(b)
40.0	16.0	13.53	0.0838	0.849	(a)
			0.357	0.611	(b)
70.0	32.0	28.88	0.0599	0.818	(a)
		28.28	0.294	0.656	(b)

At the initial stage of helium burning phase, the reaction cross section of $^{12}C(p,\gamma)^{13}N$ reaction has a great importance in understanding the exact role of ^{13}C (produced from ^{12}C through the reaction $^{12}C(p,\gamma)^{13}N$) as neutron producer. Not only that, capture of the excited ^{12}C core is also another area which needs further investigation. It has been previously mentioned that the analysis of the behaviour of $^{12}C(p,\gamma)^{13}N$ reaction in the excitation range 40–54 MeV indicates no resonant decay of ^{13}N either at ground state or at excited states except in the excited states with energies 6.36, 7.38 and 9.00 MeV. For these states the excited ^{12}C core is coupled with a single proton through two step reaction mechanisms having observable capture cross section of the order of 1.5–2.0 μb.

During this core helium burning in massive stars, the $^{12}C(\alpha,\gamma)^{16}O$ reaction competes with the triple alpha reaction and ratio of these two reaction rates finally determines the amount of ^{12}C, ^{16}O and the ratio of $^{12}C/^{16}O$ as well as the abundances of the elements produced in the later evolution of massive star after helium burning. But problem arises in determining the experimental exact value of the reaction cross section of the reaction $^{12}C(\alpha,\gamma)^{16}O$ near the astrophysically important energy $E \simeq 300$ KeV. Theoretical extrapolation of the cross section of this reaction needs the measurements at higher energies which produces insensitive data source, the radiative alpha capture cross section of ^{12}C into the ground state of ^{16}O is mostly the result of resonance.

Recent studies [101,102] of the $^{12}C(\alpha,\gamma)^{16}O$ reaction rate using the *R*- and *K*-matrix parameterizations indicate that above the α-threshold of ^{16}O the required extrapolation of the cross section to 300 keV is complicated due to interference of the components of both $l = 1$ and $l = 2$ partial waves in the cross section. It offers an indication of total cross section factor which is 62 keV barns $\leq S(300) \leq 270$ keV barns. This also gives the best estimate for the cascade transitions which is 16 keV barns bringing $S_{1,1}(300)$ to the recommended cross section of 146 keV barns. The latest result of stellar reaction rate for $^{12}C(\alpha,\gamma)^{16}O$, normalized to the reaction rate of CF88 [99], is shown in Figure 20a. The temperature dependence of this reaction rate is steeper in nature with reference to CF88. The reaction rate [for $S(300) = 100$ keV barn (CF88)

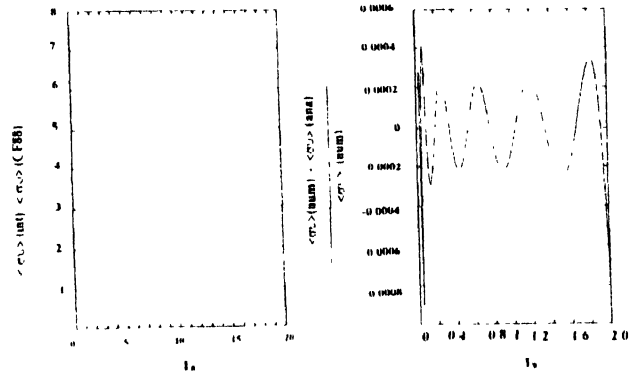

Figure 20(a) The ratio of numerically integrated stellar reaction rate for $^{12}C(\alpha,\gamma)^{16}O$ ("integrated") and that of CF88 for cross section factors S(300) of 62, 146 and 270 keV barns, respectively for temperature T_9 0.03–2.0 as obtained by Buchmann [102]. (b) The difference between the numerically integrated reaction rate ("num") of $^{12}C(\alpha,\gamma)^{16}O$ and the analytic expression ("ana") similar to those in CF88 [99] normalized to the numerically integrated rate for the recommended rate of S(300) = 146 keV barns (from Ref. 102)

is larger than the one in CF88 for temperature $T_8 > 1.8$ whereas for a lower temperature $T_8 < 1.8$ it is smaller. The computational analysis of the reaction rate by numerical integration (obtained by folding nuclear cross section with Maxwell-Boltzmann distribution [103]) and analytic integration of this reaction gives the picture of relative deviation (see Figure 20b) in the temperature range T_9 0.3 – 2.0 for the recommended value $S(300) = 146$ keV barns. It is seen from this figure :

(i) an oscillatory behaviour exists between the two rates;

(ii) at extremes, a maximum deviation of 0.09% is observed which is around 0.02% for most temperatures;

(iii) at the limits $S(300) = 62$ keV barns (lower limit), and $S(300) = 270$ keV barns (upper limit) the deviations between numerical and analytic expressions are somewhat larger ~ 1.2% in the $S(300) = 62$ keV barns at $T_9 = 0.04$ [102];

(iv) larger deviations are found for higher and lower temperatures;

(v) uncertainties in the stellar reaction rate of $^{12}C(\alpha,\gamma)^{16}O$ are larger at higher temperatures upto $T_9 = 1.5$ than at $T_9 = 0.2$.

This means that the value of the absolute cross section factor $S(300)$ and the detailed composition by partial waves of the $^{12}C(\alpha,\gamma)^{16}O$ reaction cross section are very crucial. In this case, Buchmann [102] has revised the analytical expression of reaction rate in the temperature range T_9 0.03–2.0. As it is believed that core helium burning of massive stars occurs between $T_8 = 0.15$ and 3.0 this author suggests that the revised analytic expression for the stellar reaction rate of $^{12}C(\alpha,\gamma)^{16}O$ has to be calculated in the temperature range $(0.01-0.5) \leq T_9 \leq (2.0-2.5)$ with an elaborate change covering the temperature given in the parenthesis.

The ^{12}C and ^{16}O are essentially transformed to ^{14}N in the helium core burning with an increase in central mass fraction while ^{13}C decreases to its equilibrium value, ^{18}O and ^{19}F are depleted because after the He core contraction the temperature rises to $\sim T_8$ K at which the reactions $^{13}C(\alpha,n)^{16}O$ and $^{14}N(\alpha,\gamma)^{18}F(\beta^+)^{18}O$ become active. A short burst of 10^{10} neutrons cm^{-3} yield from $^{13}C(\alpha,n)^{16}O$ while almost all the ^{14}N turn into ^{18}O through the reaction $^{14}N(\alpha,\gamma)^{18}F(\beta^+)^{18}O$ Later 3α reaction becomes active which accelerates the depletion of ^{18}O by the reaction $^{18}O(\alpha,\gamma)^{22}Ne$ that ultimately increases the abundance of ^{22}Ne. Of course, α transfer experiment [103] indicates that the contribution of low energy resonances of $^{18}O(\alpha,\gamma)^{22}Ne$ and $^{22}Ne(\alpha,n)^{25}Mg$ and the absolute uncertainties in the α-spectroscopic factors are to be considered. The neutron capture reaction $^{18}O(n,\gamma)^{19}O$ in this helium core burning has an important role because its higher energy resonances at E_R - 371, 625 and 746 keV

Table 6. Characteristics of the observed resonances in $^{18}O(\alpha,\gamma)$ and $^{18}O(n,\gamma)$ reactions (Compiled from Refs [104,105,71])

Resonance at E_R (keV)	Excitation energy E_x (MeV)	Angular distribution J^π	Resonance Strength for	
			$^{18}O(\alpha,\gamma)$ reaction $\omega\gamma_{\alpha,\gamma}$(μeV)	$^{18}O(n,\gamma)$ reaction $\omega\gamma_{n,\gamma}$(eV)
152	4 109	$3/2^+$	—	$(2.8\pm0.8)\times10^{-1}$
218	9 850	2^+	7.1×10^{-12}	
		1	5.8×10^{-11}	—
371	4 328	3/2, 5/2	- -	> 0.75
470	10.080	0^+	0.55	-
		1^-	0.23	
566	10.130	4^+	7.9×10^{-1}	-
		2^+	1.95	
		3	0.15	—
625	4 582	$3/2^-$	-	3.8 ± 0.8
662	10.210	1^-	230 ± 25	—
746	4 703	$5/2^+$	—	$1.65+0.3$

seem to correspond to neutron unbound states in ^{19}O observed in transfer reaction experiment [104]. The analysis of the observed resonance features of $^{18}O(\alpha,\gamma)$ and $^{18}O(n,\gamma)$ reactions (see Table 6) indicates that in the temperature range $(0.1-0.3)\times10^9$ K of stellar He burning the reaction rate of $^{18}O(\alpha,\gamma)$ is dominated by the resonance at 470 keV whereas for $^{18}O(n,\gamma)$ reaction the resonance at $E_R = 371$ keV is in good agreement. However, the $^{18}O(n,\gamma)$ is a fairly weak reaction and the s-process neutron flux at the stellar He burning condition is so low that sufficient reduction of ^{18}O *via* neutron capture is not possible [104,105].

The abundances of ^{16}O, ^{22}Ne are greatly modified during central He burning (α,γ) reactions and the abundance of ^{22}Ne begins to reduce towards the He exhaustion when the reaction $^{22}Ne(\alpha,\gamma)^{25}Mg$ becomes active at temperature T_8 2.5 with a huge generation of neutrons. During late He burning phase, both ^{25}Mg and ^{26}Mg increase by a factor of 50 - 100 or more through the reactions $^{22}Ne(\alpha,n)^{25}Mg(n,\gamma)^{26}Mg$ and $^{22}Ne(\alpha,\gamma)^{26}Mg$. But the abundance of ^{25}Mg is reduced by the proton capture reaction $^{25}Mg(p,\gamma)^{26}Al$ [106]. The competition between the reactions $^{25}Mg(n,\gamma)^{26}Mg$ and $^{25}Mg(p,\gamma)^{25}Al$ will affect not only the amount of excess neutrons but also the abundance of ^{26}Mg and ^{26}Al. In Table 7 we have compiled the tentative/recommended stellar reaction rate of $^{22}Ne(\alpha,n)^{25}Mg$, $^{25}Mg(p,\gamma)^{26}Al$, and $^{22}Ne(\alpha,\gamma)^{26}Mg$ reactions available in literature. In the temperature range $T_9 \leq 0.3$ the $^{22}Ne(\alpha,n)^{25}Mg$ reaction rate has a substantial enhancement due to the effect of a possibly strong 633 keV resonance with a clear uncertainty in the existence of 633 keV. In case of the $^{22}Ne(\alpha,\gamma)^{26}Mg$ reaction rate, the possible resonance of 633 keV may affect the reaction rate only slightly in the temperature range T_9 - 0.22–0.26 whereas in temperature range $T_9 \leq 0.22$ and $T_9 \leq 0.30$ the dominant role comes from the resonances at 400 keV and 828 keV, respectively [71]. The three resonances, namely, 260 keV, 96 keV and 198 keV have important role in determining the lower and upper limits of the total reaction rates of $^{25}Mg(p,\gamma)$ reaction. For a temperature T_9 - 0.02–0.15, both 60 keV and 96 keV resonances dominate the reaction rate while the observed resonances with $E_R \geq 198$ keV are effective for determining the stellar reaction rate for $T_9 > 0.15$ [104]. This present reaction rates deviate by a factor of 2 from the earlier results [108].

The recent results of network calculations for Mg -Al cycle are shown in Figure 21. The main effect of this cycle is the production of ^{26}Al though $^{25}Mg(p,\gamma)$ reaction at low temperatures and it terminates at $^{26,27}Al$, indicating as an individual reaction having the value of $^{26}Al/^{27}Al$ ratio as high as $\sim(0.38-0.95)$. The neutron densities at the center of each helium core and the relative neutron absorbers as a function of ^4He mass fraction are shown in Figures 22a,b, respectively.

4.4. Carbon burning :

Towards the end of helium exhaustion the C–O core is composed of mainly ^{16}O, ^{12}C, ^{26}Mg, ^{22}Ne, ^{20}Ne and ^{25}Mg The subsequent contraction of the C–O core causes rise of temperature and ultimately initiates the central C-burning The hydrostatic carbon burning in the temperature range $0.8 \leq T_9 \leq 1.2$ gives three main products ^{20}Ne, ^{23}Na and ^{23}Mg through the reactions $^{12}C(^{12}C,\alpha)^{20}Ne$, $^{12}C(^{12}C,p)^{23}Na$ and $^{12}C(^{12}C,n)^{23}Mg$, respectively. At lower temperatures the neutron producing reaction $^{12}C(^{12}C,n)$ is the weakest among these three [84]. The freed α, protons and neutrons can again interact with the nuclei present including CNO nuclei produced earlier. As a result, partial transformation takes place which ultimately gives a range of nuclei such as $^{20-22}Ne$, ^{23}Na, $^{24-26}Mg$, $^{26,27}Al$, $^{28-30}Si$, ^{31}P, *etc* But the main transformed product is ^{24}Mg produced through the reaction $^{20}Ne(\alpha,\gamma)^{24}Mg$ and $^{23}Na(p,\gamma)^{24}Mg$

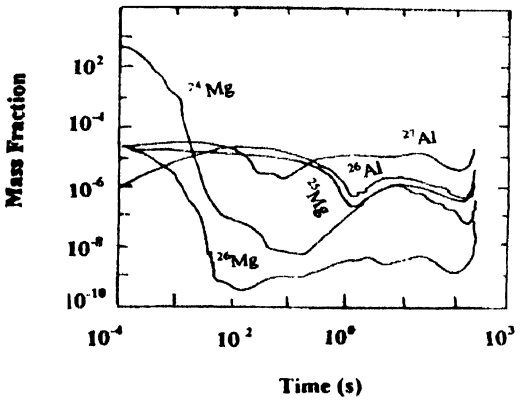

Figure 21. Time evolution of mass fraction for $T_9 = 0.3$, $\rho = 600$ g cm^{-3} for Mg–Al reactions as obtained by G M Hale [109]

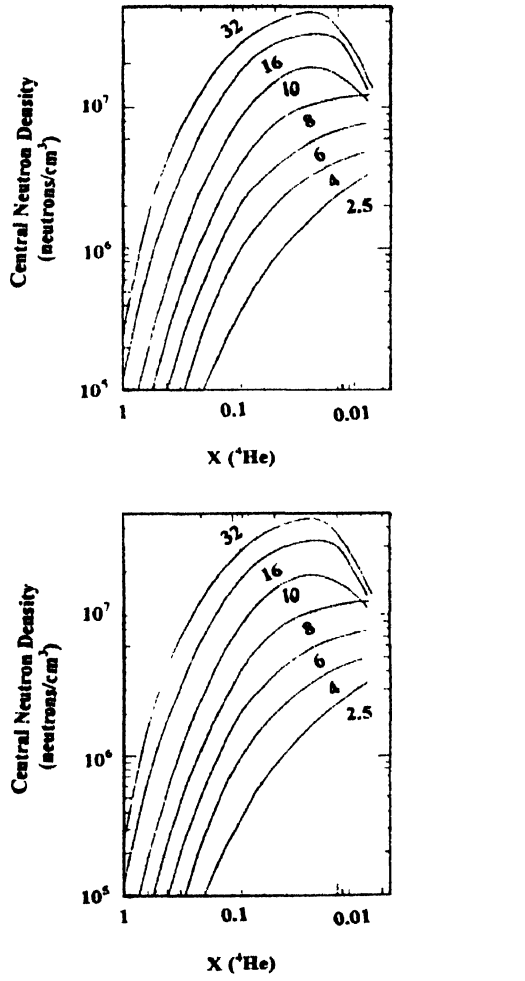

Figure 22. (a) The neutron densities at the center for each helium core as a function of ^{4}He mass fraction (b) Relative contributions of various neutron absorbers as a function of ^{4}He mass function for helium core $M_\alpha = 16\ M_\odot$ (from Ref. [100]).

When C is depleted in the centre, an O–Ne core with relatively homogeneous chemical composition is formed This core has a very small amount of neutrons because of the lack of strong neutron sources. In this phase the important neutron source, $^{22}Ne(\alpha,n)$ reaction is less effective because of non-availability of sufficient α-particles. On the other hand, the chain reaction $^{20}Ne(n,\gamma)^{21}Ne(\alpha,n)^{25}Mg$ turns into a self-limited neutron source because of neutron capture by ^{20}Ne and ^{25}Mg.

The He shell burning during this phase, dominates ^{12}C and ^{16}O at the bottom of the shell The partial He burning in the He shell may produce the important nuclei ^{19}F through the reactions $^{18}O(p,\gamma)^{15}N(\alpha,\gamma)^{19}F$ in which the required protons and neutrons are supplied by $^{14}N(n,p)^{14}C$ and $^{13}C(\alpha,n)^{16}O$ reactions, respectively Thus for production of ^{19}F the condition of co-existence of ^{13}C, ^{14}N and ^{18}O is necessary in the early He-burning [111] Recently, Aubert *et al* [110] found in an investigation that ^{19}F is produced through the chain reaction $^{14}N(n,\gamma)^{15}N(\alpha,\gamma)^{19}F$ even before the production of ^{18}O at low temperature condition Although the $^{14}N(n,\gamma)^{15}N$ reaction is much slower than the $^{14}N(n,p)^{14}C$, the production of ^{19}F by the abundant ^{14}N through leakage in this He shell burning gives rise to another interesting problem.

4.5 Neon burning

At the end of carbon burning the core nuclei are mainly ^{16}O, ^{20}Ne and ^{24}Mg. Since the temperature at this stage is high enough (*i.e.* $T_9 \geq 1.2$), photo-disintegration takes place in ^{20}Ne *via* the reaction $^{20}Ne(\gamma,\alpha)^{16}O$ before the oxygen burning and produces large amount of α-particles Part of these freed alpha particles are captured by ^{16}O through the inverse reaction $^{16}O(\alpha,\gamma)^{20}Ne$ and part by the reaction chain $^{20}Ne(\alpha,\gamma)^{24}Mg(\alpha,\gamma)^{28}Si$, $^{24}Mg(\alpha,\gamma)^{27}Al$. The competitive reactions $^{24}Mg(\alpha,\gamma)^{28}Si$, ^{27}Al ultimately enhances the abundances of ^{24}Mg, ^{27}Al and to a smaller extent of ^{28}Si at the central Ne exhaustion. The other dominating nuclei at the end of this central Ne burning are ^{24}Mg, ^{32}S, $^{25,26}Mg$, $^{29,30}Si$ and ^{31}P.

The interesting feature in the convective C-burning shell in this phase is the existence of the large area of expanding

Table 7. Stellar reaction rate for $^{22}Ne(\alpha,n)^{25}Mg$, $^{25}Mg(p,\gamma)^{26}Al$, $^{22}Ne(\alpha,\gamma)^{26}Mg$

Temperature	$^{22}Ne(\alpha,n)^{25}Mg$			$^{25}Mg(p,\gamma)^{26}Al$			$^{22}Ne(\alpha,\gamma)^{26}Mg$		
T_9	Tentative/ Recommended value	Upper limit	Lower limit	Tentative/ Recommended value	Upper limit	Lower limit	Tentative/ Recommended value	Upper limit	Lower limit
0.01	—	—	—	3.47×10^{-34}	7.74×10^{-31}	4.19×10^{-34}	—	—	—
0.02	—	—	—	3.79×10^{-20}	4.47×10^{-20}	4.42×10^{-20}	—	—	—
0.03	—	—	—	1.39×10^{-15}	1.61×10^{-15}	1.61×10^{-15}	—	—	—
0.04	—	—	—	2.39×10^{-13}	2.75×10^{-13}	2.75×10^{-13}	—	—	—
0.05	—	—	—	5.27×10^{-12}	6.17×10^{-12}	6.17×10^{-12}	—	—	—
0.06	5.02×10^{-46}	1.00×10^{-45}	3.61×10^{-57}	4.78×10^{-11}	5.83×10^{-11}	5.83×10^{-11}	8.61×10^{-36}	1.00×10^{-34}	8.72×10^{-37}
0.07	—	—	—	2.76×10^{-10}	3.54×10^{-10}	3.53×10^{-10}	—	—	—
0.08	5.61×10^{-35}	1.12×10^{-34}	1.23×10^{-42}	1.16×10^{-9}	1.55×10^{-9}	1.59×10^{-9}	7.35×10^{-29}	8.55×10^{-28}	7.45×10^{-30}
0.09	—	—	—	3.81×10^{-9}	5.19×10^{-9}	5.15×10^{-9}	—	—	—
0.10	2.21×10^{-28}	4.42×10^{-28}	5.99×10^{-34}	1.05×10^{-8}	1.44×10^{-8}	1.42×10^{-8}	9.83×10^{-25}	1.14×10^{-23}	9.95×10^{-26}
0.12	5.24×10^{-24}	1.05×10^{-23}	3.53×10^{-28}	—	—	—	5.27×10^{-21}	6.21×10^{-21}	5.33×10^{-23}
0.14	6.75×10^{-21}	1.35×10^{-20}	4.50×10^{-24}	—	—	—	4.57×10^{-20}	5.26×10^{-19}	4.58×10^{-21}
0.15	—	—	—	5.94×10^{-6}	5.51×10^{-6}	5.49×10^{-6}	—	—	—
0.16	1.42×10^{-18}	2.83×10^{-18}	5.25×10^{-21}	—	—	—	1.35×10^{-18}	1.46×10^{-17}	1.27×10^{-19}
0.18	8.97×10^{-17}	1.78×10^{-16}	1.25×10^{-18}	—	—	—	2.30×10^{-17}	1.99×10^{-16}	1.86×10^{-18}
0.20	2.49×10^{-15}	4.89×10^{-15}	9.80×10^{-17}	1.23×10^{-3}	1.11×10^{-3}	1.11×10^{-3}	3.25×10^{-16}	1.77×10^{-15}	3.14×10^{-15}
0.25	1.14×10^{-12}	2.05×10^{-12}	2.40×10^{-13}	—	—	—	1.22×10^{-13}	2.80×10^{-13}	4.74×10^{-14}
0.30	9.09×10^{-11}	1.44×10^{-10}	4.14×10^{-11}	2.51×10^{-1}	2.44×10^{-1}	2.44×10^{-1}	1.22×10^{-11}	1.63×10^{-11}	8.06×10^{-12}
0.35	2.58×10^{-9}	3.67×10^{-9}	1.60×10^{-9}	—	—	—	3.93×10^{-10}	4.74×10^{-10}	3.08×10^{-10}
0.40	3.47×10^{-8}	4.65×10^{-8}	2.43×10^{-8}	3.32	3.67	3.67	5.53×10^{-9}	6.42×10^{-9}	4.80×10^{-9}
0.50	1.53×10^{-6}	1.92×10^{-6}	1.15×10^{-6}	1.75×10^{1}	1.93×10^{1}	1.93×10^{1}	2.22×10^{-7}	2.51×10^{-7}	1.92×10^{-7}
0.60	2.57×10^{-5}	3.21×10^{-5}	1.93×10^{-5}	5.43×10^{1}	5.98×10^{1}	5.98×10^{1}	2.52×10^{-6}	2.83×10^{-6}	2.21×10^{-6}
0.70	—	—	—	1.24×10^{2}	1.36×10^{2}	1.36×10^{2}	—	—	—
0.80	2.59×10^{-3}	3.34×10^{-3}	1.89×10^{-3}	2.32×10^{2}	2.55×10^{2}	2.55×10^{2}	5.16×10^{-5}	5.75×10^{-5}	4.56×10^{-5}
0.90	—	—	—	3.81×10^{2}	4.18×10^{2}	4.18×10^{2}	—	—	—
1.00	7.11×10^{-2}	9.25×10^{-2}	5.27×10^{-2}	5.71×10^{2}	6.24×10^{2}	6.24×10^{2}	3.64×10^{-4}	4.03×10^{-4}	3.22×10^{-4}

Compiled from References [71, 104, 107]

shell which will be affected by the subsequent presupernova and explosive nucleosynthesis. To what extent the ^{26}Al nuclei will be affected is not yet clear.

4.6. Oxygen burning :

Towards the end of Ne burning the core temperature $T_9 \sim 2.0$ favours the oxygen burning which releases α-particles, protons and neutrons during this burning period *via* the reaction :

$$^{16}O + {}^{16}O \rightarrow {}^{28}Si + \alpha,$$
$$\rightarrow {}^{31}P + p,$$
$$\rightarrow {}^{31}S + n,$$
$$\rightarrow {}^{30}Si + 2p.$$

These α-particles, protons and neutrons then interact with the nuclei present in the core and give a large spread of nuclei such as ^{28}Si, $^{32\text{-}34}Si$, $^{35,37}Cl$, $^{36,38}Ar$, $^{39,41}K$, $^{40,42}Ca$, ^{46}Ti, ^{50}Cr, *etc* and an increase in neutron excess from 2×10^{-3} to $\sim 6 \times 10^{-3}$ during the core oxygen burning [112]. Here the main problemis disagreement of these large atomic number nuclei with observation, *i.e.* all the above mentioned large spread of nuclei produced in the core oxygen burning, are not detected in observation. One of the reasons is that the product nuclei of core oxygen burning are very rarely ejected in the interstellar medium (ISM).

4.7. Silicon burning :

In the silicon burning phase, the core silicon burning begins at about a temperature $T_9 = 2.7$ through photo-disintegration of the nuclei produced in the previous burning processes. As the binding energies for protons, neutrons and alpha particles in ^{32}S are lower than that in ^{28}Si, the nuclei ^{32}S will be the first to photo-disintegrate *via* the (γ–p) and (γ–n) processes :

$$^{32}S + \gamma \rightarrow {}^{31}P + p - 8.864 \text{ MeV},$$
$$^{31}P + \gamma \rightarrow {}^{30}Si + p - 7.287 \text{ MeV},$$

$^{30}Si + \gamma \rightarrow {}^{29}Si + n,$

$^{29}Si + \gamma \rightarrow {}^{28}Si + n.$

The neutron excess per nucleon and temperature, both increases with time as the reaction process advances and finally the build up nuclei of the core reach the iron peak, the most abundant nuclei of which are likely to be ^{54}Fe, ^{56}Fe and ^{58}Ni. During core silicon burning, helium, carbon and oxygen shell burnings also take place while neutronization of the core proceeds significantly.

4.8. Presupernova yields :

Table 8 shows the presupernovae yields for various helium star masses M_α = 3.3, 4, 5, 6, 8, 16 and 32 $M_\odot$ (the corresponding main sequence masses M_{ms} = 13, 15, 18, 20, 25, 40 and 70 $M_\odot$, respectively). Recent analysis [113] of the isotopic abundances, obtained through averaging over the mass range 10–50 $M_\odot$ with an initial mass function $\propto M^{1.35}$ relative to their solar values, indicates that for $A < 27$ the relative abundances of massive stars are in good agreement with the solar values. For 25 $M_\odot$ the yields of Ne, Na and Al show an over production compared to the solar ratio. It seems that this is due to the $^{12}C(\alpha,\gamma)^{16}O$ reaction rate which is higher than that of the CF88 values. Experimentally measured values of reaction rate of $^{12}C(\alpha,\gamma)^{16}O$, which lies in between the rates of CF88 and CFHZ85, suggest the dependence of isotopic ratio on the reaction rate of $^{12}C(\alpha,\gamma)$. Not only that, convective overshooting and requirement of fresh He in the core for late stage high temperature core helium burning are also important factors to be considered. Some species underproduced relative to their solar values such as ^{35}Cl, ^{39}K, ^{44}Ca, ^{48}Ti and ^{59}Co show an enhancement by a factor of ~2 for ^{35}Cl, ^{39}K and ^{44}Ca as well as appreciable enhancement for ^{48}Ti and ^{59}Co in contrast to the solar seed abundances when the s-process weak component nuclei $50 < A < 100$ are under consideration during core helium burning. This means much attention is required towards the $^{12}C(\alpha,\gamma)^{16}O$ reaction rate.

4.9 Supernova phase

In the above, we see that a large number of species are produced during the helium core mass evolution from helium burning to Fe core formation. It is also believed that

(i) among these nuclear species ^{18}F, produced through reaction $^{14}N(\alpha,\gamma)^{18}F$ is quickly transformed into ^{18}O *via* β^+ decay *i.e.* produced by (p,γ) reaction,

(ii) ^{23}Mg, ^{27}Si, ^{29}P, $^{33,34}Cl$ are quickly transformed to their decay product,

(iii) $^{33,35}P$ are transformed into ^{33}S and ^{35}P *via* the reaction (p,n).

However, prior to collapse, the core of the massive star largely consists of ^{54}Fe and other neutron rich isotopes which are the ashes of silicon burning. Further collapse of the core of the massive star gives birth of a neutron star with the release of a huge flux of neutrinos. In this stage, the cross sections for collision are small, yet there are many neutrinos which excite the heavy elements, the de-excitation of which are likely to emit protons, neutrons or alpha particles. It is also believed that the energy input by these neutrinos favours their diffusion out of the collapsed central part of the star and ultimately drives the explosion of type II supernova on a time scale of about a second, the so called neutrino driven "delayed explosion" [114]. Recent observations and numerical calculations indicate that this neutrino driven mechanism does not play a dominant role. In investigating the synthesis of heavy elements using the numerical models. Witti [115] found a successful r-process caused by the neutrino driven radiative entropy whose magnitude is low by a factor of ~4 in type II supernova explosion. Observations of low abundance or deficit of B nuclei (by 250%) [116] and O rich (by 60%) [117] environment in the vicinity of massive supernova are in contrast with the production of sufficient B and Be nuclei through spallation by low energy C and O atoms onto protons and alpha particles. Only more investigations can help us to solve this neutrino r-process problem in type II supernova explosion mechanism.

Table 8. Presupernova yields for various progenitor masses *H*-rich envelope is not included (after, Nomoto *et al* [113])

Species	Synthesized isotopic mass ($M_\odot$)						
	m = 13 $M_\odot$	m = 15 $M_\odot$	m = 18 $M_\odot$	m = 20 $M_\odot$	m = 25 $M_\odot$	m = 40 $M_\odot$	m = 70 $M_\odot$
^{12}C	2.68E–03	8.26E–02	1.65E–01	1.14E–01	1.48E–01	1.48E–01	4.67E–01
^{13}C	9.47E–09	4.97E–10	7.73E–10	1.17E–10	1.03E–08	3.02E–10	2.57E–10
^{14}N	3.75E–08	5.37E–03	3.39E–03	2.72E–03	9.53E–04	7.08E–05	7.68E–03
^{15}N	2.08E–08	1.36E–10	9.05E–08	6.48E–10	1.04E–08	1.19E–08	2.36E–10
^{16}O	1.51E–01	3.55E–01	7.92E–01	1.48	2.99	9.11	2.14E+01
^{17}O	6.07E–08	4.41E–09	4.01E–07	9.86E–09	7.86E–08	3.13E–07	6.64E–10
^{18}O	9.44E–09	1.35E–02	8.67E–03	8.68E–03	6.69E–03	1.79E–06	3.80E–03
^{19}F	8.06E–10	2.12E–11	7.67E–09	7.84E–11	8.17E–10	7.38E–10	2.63E–15
^{20}Ne	2.25E–02	2.08E–02	1.61E–01	2.29E–01	5.94E–01	6.58E–01	2.00
^{21}Ne	2.08E–04	3.93E–05	2.19E–03	3.03E–04	3.22E–03	2.36E–03	1.14E–02
^{22}Ne	1.01E–04	1.25E–02	2.74E–02	2.93E–02	3.93E–02	5.66E–02	5.23E–02

Table 8. *(Cont'd)*

Species	Synthesized isotopic mass ($M_\odot$)						
	m = 13 $M_\odot$	m = 15 $M_\odot$	m = 18 $M_\odot$	m = 20 $M_\odot$	m = 25 $M_\odot$	m = 40 $M_\odot$	m = 70 $M_\odot$
^{23}Na	7.27E-04	1.53E-04	7.25E-03	1.15E-03	1.81E-02	2.37E-02	6.98E-02
^{24}Mg	9.23E-03	3.16E-02	3.62E-02	1.47E-01	1.59E-01	3.54E-01	7.87E-01
^{25}Mg	1.38E-03	2.55E-03	7.54E-03	1.85E-02	3.92E-02	4.81E-02	1.01E-01
^{26}Mg	8.96E-04	2.03E-03	5.94E-03	1.74E-02	3.17E-02	1.07E-01	2.91E-01
^{27}Al	1.04E-03	4.01E-03	5.44E-03	1.55E-02	1.95E-02	8.05E-02	1.44E-01
^{28}Si	6.68E-02	7.16E-02	8.69E-02	8.50E-02	1.03E-01	4.29E-01	7.55E-01
^{29}Si	7.99E-04	3.25E-03	1.76E-03	9.80E-03	6.97E-03	5.43E-02	1.08E-01
^{30}Si	1.87E-03	4.04E-03	3.33E-03	7.19E-03	6.81E-03	4.32E-02	1.00E-01
^{31}P	2.95E-04	6.55E-04	4.11E-04	1.05E-03	9.02E-04	5.99E-03	2.57E-02
^{32}S	1.46E-02	3.01E-02	3.76E-02	2.29E-02	3.84E-02	1.77E-01	2.05E-01
^{33}S	1.19E-04	9.60E-05	1.48E-04	8.84E-05	2.20E-04	7.49E-04	1.02E-03
^{34}S	1.83E-03	1.49E-03	1.89E-03	1.26E-03	2.77E-03	1.14E-02	1.98E-02
^{36}S	3.04E-07	3.34E-07	8.08E-07	4.23E-07	7.51E-07	1.40E-05	2.17E-06
^{35}Cl	3.70E-05	3.45E-05	8.95E-05	6.05E-05	6.72E-05	4.75E-04	1.76E-03
^{37}Cl	6.73E-06	9.60E-06	1.04E-05	4.96E-06	1.32E-05	1.17E-04	1.01E-04
^{36}Ar	2.36E-03	5.63E-03	6.13E-03	3.78E-03	6.71E-03	3.11E-02	2.92E-02
^{38}Ar	4.85E-04	6.49E-04	6.29E-04	3.25E-04	7.24E-04	9.14E-03	6.16E-03
^{40}Ar	4.82E-09	3.24E-09	1.42E-08	4.65E-09	8.92E-09	1.74E-07	5.07E-08
^{39}K	1.95E-05	3.31E-05	3.66E-05	3.24E-05	3.47E-05	3.83E-04	3.84E-04
^{41}K	1.42E-06	2.37E-06	2.23E-06	1.28E-06	2.79E-06	3.43E-05	2.84E-05
^{40}Ca	2.53E-03	5.29E-03	5.11E-03	3.25E-03	6.15E-03	2.56E-02	2.14E-02
^{42}Ca	1.02E-05	1.63E-05	1.45E-05	9.45E-06	1.77E-05	3.13E-04	1.64E-04
^{43}Ca	1.91E-06	1.30E-06	3.99E-07	3.38E-06	2.78E-07	4.02E-07	4.09E-06
^{44}Ca	1.22E-04	7.49E-05	1.43E-05	9.15E-05	2.11E-05	2.00E-05	2.97E-04
^{46}Ca	2.06E-10	6.23E-11	3.23E-11	1.12E-11	2.60E-10	4.39E-10	2.23E-10
^{48}Ca	1.13E-13	3.99E-16	1.07E-15	2.41E-16	1.70E-14	2.48E-13	2.36E-14
^{45}Sc	4.26E-08	7.44E-08	1.18E-07	1.04E-07	8.96E-08	1.53E-06	2.78E-06
^{46}Ti	2.56E-06	6.26E-06	6.72E-06	6.81E-06	6.84E-06	3.56E-05	1.44E-05
^{47}Ti	5.13E-06	3.75E-06	3.11E-07	1.73E-06	9.11E-07	9.74E-07	6.26E-07
^{48}Ti	1.68E-04	1.58E-04	8.59E-05	1.85E-04	8.98E-05	1.58E-04	1.42E-04
^{49}Ti	3.45E-06	6.10E-06	7.54E-06	4.89E-06	6.01E-06	2.17E-05	6.97E-06
^{50}Ti	3.56E-10	1.21E-09	1.17E-10	1.12E-10	5.90E-10	2.00E-10	2.56E-10
^{50}V	8.65E-10	8.57E-10	4.64E-10	2.15E-10	7.99E-10	2.14E-09	1.52E-09
^{51}V	9.34E-06	1.25E-05	1.25E-05	6.40E-06	9.96E-06	2.73E-05	1.15E-05
^{50}Cr	2.30E-05	5.15E-05	7.49E-05	3.54E-05	5.01E-05	1.49E-04	1.01E-04
^{52}Cr	1.15E-03	1.36E-03	1.44E-03	8.64E-04	1.31E-03	2.77E-03	6.86E-04
^{53}Cr	9.34E-05	1.35E-04	1.50E-04	7.12E-05	1.39E-04	3.56E-04	1.00E-04
^{54}Cr	3.35E-08	4.09E-08	2.53E-08	6.26E-09	2.41E-08	2.81E-08	7.61E-08
^{55}Mn	3.65E-04	4.74E-04	5.48E-04	2.27E-04	5.02E-04	8.41E-04	3.64E-04
^{54}Fe	2.10E-03	4.49E-03	6.04E-03	2.52E-03	4.81E-03	9.17E-03	5.81E-03
^{56}Fe	1.50E-01	1.44E-01	7.57E-02	7.32E-02	5.24E-02	7.50E-02	7.50E-02
^{57}Fe	4.86E-03	4.90E-03	2.17E-03	3.07E-03	1.16E-03	2.29E-03	3.83E-03
^{58}Fe	3.93E-09	1.27E-08	1.37E-08	3.70E-09	8.34E-09	1.29E-08	4.17E-08
^{59}Co	1.39E-04	1.22E-04	4.82E-05	1.31E-04	2.19E-05	2.51E-05	1.59E-04
^{58}Ni	5.82E-03	7.50E-03	3.08E-03	3.71E-03	1.33E-03	3.31E-03	9.25E-03
^{60}Ni	3.72E-03	3.36E-03	8.71E-04	2.18E-03	6.67E-04	3.88E-04	1.77E-03
^{61}Ni	1.58E-04	1.43E-04	4.77E-05	1.59E-04	2.75E-05	2.57E-05	1.55E-04
^{62}Ni	1.05E-03	9.50E-04	2.52E-04	7.26E-04	1.70E-04	1.11E-04	1.28E-03
^{64}Ni	2.02E-15	4.28E-15	2.93E-16	2.06E-15	6.08E-15	6.49E-16	4.33E-12
^{63}Cu	1.18E-06	1.01E-06	4.32E-07	3.00E-06	1.50E-07	1.62E-07	9.09E-06
^{65}Cu	9.11E-07	7.17E-07	8.40E-08	7.02E-07	1.42E-07	1.89E-08	5.34E-07
^{64}Zn	2.14E-05	1.99E-05	3.89E-06	1.78E-05	3.10E-06	8.79E-07	1.02E-05
^{66}Zn	1.63E-05	1.30E-05	4.47E-06	2.08E-05	2.58E-06	9.99E-07	3.09E-05
^{67}Zn	2.13E-08	1.54E-08	3.39E-09	6.39E-08	2.95E-09	2.51E-10	1.95E-07
^{68}Zn	6.63E-09	7.35E-09	8.36E-10	5.33E-09	9.29E-10	1.20E-10	9.51E-08

Table 9. Various unsolved problems of neutron capture nucleosynthesis remaining for further investigation

Phase		Problems/constraints
Birth of the star	(1)	The behaviour of molecular gas formation/gravitationally bound cloud formation as a crucial regulator of star formation the question is which one controls the star formation
	(2)	Accurate determination of gas density and growth rate of clouds
	(3)	The missing link between the dense molecular cloud cores and embedded pre-main sequence stars
	(4)	How much portion of the collapsing molecular clouds forms a star?
Hydrogen burning		
Helium core burning	(5)	Measurement of $^{13}C/^{12}C$ and of $^{13}N(n,\gamma)^{14}N$ reaction rate Competition of $^{13}N(p,\gamma)^{14}O$ reaction with $^{13}C(\alpha,n)^{16}O$ ultimately reduces the neutron production and efficiency of heavy elements synthesis
	(6)	Reaction rate of $^{22}N(\alpha,n)^{25}Mg$ at low energies as well as its uncertainties
	(7)	Possible existence of oxygen isotopes (^{17}O *etc*) just below the α-threshold of $^{13}C(\alpha,n)^{16}O$ reaction
	(8)	Possibility of rotational mixing It arises as the ratios of $^3He/^1H$, $^{14}N/^{13}C$ and $^{14}N/^{16}O$ are found to be rather large at the surfaces of fully mixed star models Even in the fully mixed rotational model enrichment of helium and nitrogen and depletion of carbon and oxygen are possible
	(9)	Exact measurement of low energy resonances for the reactions $^{21}Ne(\alpha,n)^{24}Mg$ $^{18}O(\alpha,n)^{21}Ne$ and $^{17}O(\alpha,n)^{20}Ne$
	(10)	Interpretation of the ratio $(^{16}O/^{18}O)/^{16}O/^{17}O)$ in red giant stars The first and second dredge up during the star's red giant phase contribute a minor increase in the $(^{16}O/^{18}O)$ ratio while the third dredge up gives a huge increase of $^{16}O/^{18}O$ On the other hand ^{17}O is produced only in deep layers of the star in a sufficiently high temperature environment with a high destruction possibility of it by the $^{17}O(p,\gamma)^{18}F$ and $^{17}O(p,\alpha)^{14}N$ reaction in massive stars
	(11)	Experimental verification of the rate of $^{17}O(p,\alpha)^{14}N$ reaction for determining the rate accurately
	(12)	Thorough observation regarding the correlation between strongly variable O and Na abundances
Carbon burning — Core	(13)	Large uncertainties in the $^{12}C(\alpha,\gamma)^{16}O$ reaction rate and overall production problem At the beginning of the carbon burning the neutron density is so high ($\sim 10^{11}$ cm^{-3}) that a depletion of ^{63}Cu appears due to strongly favourable situation of neutron capture by ^{63}Ni while the s-process occurring in the He core burning at stellar interior supplies an average neutron density 10^6 cm^{-3} This means that ^{63}Ni (progenitor of ^{63}Cu) and ^{64}Ni are weakly produced This weak production of ^{63}Ni ^{64}Ni as well as large uncertainty in the $^{12}C(\alpha,\gamma)^{16}O$ reaction rate need more investigation whether it is due to uncertainty in other main s-component or not Recent comparison [118] of the upgraded data for p-wave S-factor of the $^{12}C(\alpha,\gamma)^{16}O$ reaction with the other existing values of S-factor indicates that the disagreement in the S-factor of this reaction still remains
— He shell	(14)	Non-standard mixing and chemical discontinuity Theoretical calculations indicate that a chemical discontinuity arises due to convective envelope when hydrogen shell burning reaches its maximum event while observations suggest CNO element anamolies in star's chemical composition will affect the star's mass
	(15)	Exact abundances of ^{13}C and ^{22}Ne in helium burning shell
	(16)	Production of ^{19}F by the abundant 14N through leakage In the early He-shell burning the essential condition for production of ^{19}F is the co-existence of ^{13}C, ^{14}N and ^{18}O whereas recent investigation indicates the production of ^{19}F through the chain reaction $^{14}N(n,\gamma)^{15}N(\alpha,\gamma)^{19}F$ even before that of ^{18}O at low temperature condition
Oxygen burning	(17)	During the convective C-shell burning ^{26}Al exists covering a large region upto $M_r = 3.8\ M_\odot$ The effect of subsequent pre-supernova and explosive nucleosynthesis on this ^{26}Al is not yet clear
	(18)	Disagreement of the large spread of nuclei with observation
	(19)	Measurement of screening by oxygen during carbon shell burning
Silicon burning		
Supernova phase	(20)	Although neutrino driven "delayed mechanism" favours the explosion of type II supernova still some uncertainties about it remain
	(21)	The exact role of electron capture rates of fp shell nuclei, weak interaction rates and half life of very neutron rich β-decay nuclei far away from the line of stability on the pre-supernova and supernova evolution [119]
Explosion phase	(22)	The exact electron fraction Y_e required by the r-process at the boundary between the matter that escapes into the space from supernova and the matter that remains as part of the remnant neutron star
Neutron star phase	(23)	According to the Relativistic Mean Field (RMF) theory the r-process nuclei are available even far from the stability line because the neutron magic shells (*i.e* N = 82, 128) stay at those numbers which are also the same at the standard magic numbers Simultaneously, disappearence of many proton magic numbers at the neutron numbers far away from the magic numbers is also possible due to deformation As a result the proton fraction at the centre of neutron star is more than that of the conventional [120] Investigation regarding the role of proton fraction, neutrino reaction rate, *etc* for supernova evolution are very important

Table 9. *(Cont'd)*

Phase	Problems/constraints
Problems on overall burning phases	
	(24) Accurate measurement of neutron density at various burning phases During core He burning a low neutron density favours the decay of Ni isotopes (*i.e* ^{63}Ni, ^{63}Cu, .) while high neutron density in the beginning of carbon burning phase causes a depletion of ^{63}Cu due to strong neutron capture by ^{63}Ni
	(25) Search for a production mechanism of relatively light ($A \leq 80$) r-process nuclei.
	(26) Investigation of O/Fe ratio for various stars
	(27) As the $(\gamma,n) \leftrightarrows (n,\gamma)$ equilibrium location depends on the reaction Q values, the mass and nuclear structure of very neutron rich heavy nuclei (*i.e.* r-process abundances) play crucial role for understanding all the features of the r-process [121]
	(28) The intense neutrino wind from nascent neutron star can take part in nucleosynthesis with the available abundant heavy nuclei whereas the same heavy nuclei may be produced in the α-rich freeze out *via* successive neutrino induced interactions As the α-rich freeze out does not depend on the pre-existing seed nuclei but produces required primary r-process abundances, the exact ability of α-rich freeze out to produce considerable amount of massive seed nuclei (than the Fe nuclei) in order to differentiate the r-process from it.

5. Conclusion and outlook

The discussion of the preceding sections demonstrates that neutron production and its flow through different burning phases play an important role in neutron capture nucleosynthesis of elements during stellar evolution. With the help of the implementation of New Reaction Rates, hydrodynamical techniques and numerical simulations we have achieved a better understanding of nucleosynthesis after solving various constraints in it. Still various difficulties and uncertainties remain. We have presented major difficulties and constraints in various burning phases in Table 9 which will give the direction of future investigations. We are hopeful that there will be a lot of improvements in the physics of stellar nucleosynthesis through future investigations both theoretically and experimentally.

Acknowledgment

The author is grateful to the anonymous referees and the Editorial Desk of this journal for their joint efforts for correcting the manuscript and their valuable suggestions for improvement of this paper.

He is very much grateful to the Director and S C Rath, Librarian, Institute of Physics, Bhubaneswar for their kind permission to use the library facilities. It is with much pleasure that the author thanks Professor H N K Sarma, Department of Physics, Manipur University, and the staff of ACS Imphal Airport and ACS Bhubaneswar Airport for constant encouragement. He is grateful to the staff of Institute of Physics Library, Bhubaneswar, Manipur University Library, Imphal; Tata Institute of Fundamental Research Library, Mumbai; Inter University Center for Astronomy and Astrophysics Library, Pune; NCRA Library, Pune; Indian Association for the Cultivation of Science Library, Calcutta; Physical Research Laboratory, Ahmedabad; MPIA, MPIE & ESO Libraries, Garching, Germany; NORDITA Library, Copenhagen; JILA Library, Colorado; and ICTP Library, Trieste for their kind help for sending the required journal papers. The author is deeply indebated to Professor D L Lambert, Prof. J E Norris, Prof. L Buchman, Prof. Y Nagai, Prof. G Wallerstein, Prof. I Iben, Prof. W C Haxton, Prof. M Hashimoto and other Professors for kindly providing the reprints of their own works. He is also thankful to Mrs. Tapati Parui and Rajarshee Parui for their various help during the preparation of this manuscript.

References

[1] R K Parui *Indian J Phys* **67B** 109 (1993) (Paper I)

[2] R K Parui *Indian J. Phys* **69B** 1 (1995) (Paper II)

[3] R K Parui *Indian J Phys* **71B** 421 (1997) (Paper III)

[4] E M Burbidge, G R Burbidge, W A Fowler and F Hoyle *Rev. Mod Phys.* **29** 547 (1957)

[5] M Arnould and K Takahashi in *Origin and Evolution of the Elements* eds N Prantozos, E Vangioni-Flam and M Casse (Cambridge, UK Cambridge Univ Press) p395 (1993)

[6] S Ramaduari *Adv Space Res* NORDITA Preprint No 94/47A (1995)

[7] B S Meyer *Ann Rev Astron. Astrophys.* **32** 153 (1994), S Goriely *Astron Astrophys* **327** 845 (1997), K Wisshak, F Voss and F Kappeler *Phys Rev* **C57** 391, 3452 (1998)

[8] J Truran and I Iben (Jr) *Astrophys. J* **216** 797 (1977)

[9] F Kappeler, H Beer and K Wisshak *Rep Prog. Phys* **52** 945 (1989)

[10] J R Wilson and R W Mayle *Phys Reports* **227** 97 (1993)

[11] S E Woosley, G J Mathews, J R Wilson, R D Hoffman and B S Meyer *Astrophys J* **433** 229 (1994)

[12] G Wallerstein, A D Vanture, E B Jenkins and G M Fuller *Astrophys. J* **449** 688 (1995)

[13] E Anders and N Grevesse *Geochim Cosmochim Acta* **53** 197 (1989), N Grevesse *et al* in *Cosmic Abundances* eds. S Holt and G Sonebom *ASP Conf Series* **99** 117 (1996)

[14] M Hashimoto *Prog. Theor. Phys* **94** 663 (1995)

[15] F Kappeler, B Gallino, M Busso, G Picchio and C M Raiteri *Astrophys J* **354** 630 (1990)

[16] F Kappeler in *Nuclei in the Cosmos Berlin* : ed. H Oberhummer (Springer-Varlag) p.179 (1991)

[17] F Kappeler, W Schanz, K Wisshak and G Reffo *Astrophys. J.* **410** 370 (1993)

[18] J R de Lateer *Astrophys. J* **434** 695 (1994)

[19] F-K Thielemann, J-P Bitouzet, K-L Kratz, P Moller, J J Cowan and J W Truran *Phys. Rep.* **227** 269 (1993), R Surman and J Engel *Phys. Rev.* **C58** 2526 (1998); H Schatz *et al Phys Rep* **294** 168 (1998)

[20] K-L Kratz, V Harms, W Hillebrandt, B Pfeifer, F-K Thielemann and A Wohr *Z. Phys.* **A336** 357 (1990)

[21] K-L Kratz, H Gabelmann, P Moller, B Pfieffer, H L Ravn and A Wohr The ISOLDE Collaboration *Z Phys* **A340** 419 (1991)

[22] P Moller, J R Nix and K-L Kratz in *Proc Int Conf on Exotic Nuclei* (South Crimea) (1992)

[23] P Moller and J Randrup *Nucl. Phys* **A514** 1 (1990)

[24] B Pfeffer, P Moller and K-L Kratz *Table of QRPA Predictions of $T_{1/2}$ and P_n* (1991) (unpublished)

[25] K-L Kratz, F-K Thieleman, W Hillebrandt, P Moller V Harms, A Wohr and J W Truran *J. Phys* **G14** 331 (1988)

[26] W M Howard and P Moller *Atomic Data and Nucl Data Tables* **25** 219 (1980); K Takahashi, Myamada and Z Kondo *Atomic Data and Nucl. Data Tables* **12** 101 (1993)

[27] V V Smith and D L Lambert *Astrophys J. Suppl* **72**, 387 (1990)

[28] A G W Cameron, J J Cowan and J W Truran *Astrophys. Space Sci* **91** 235 (1983)

[29] B S Meyer and J S Brown *Astrophys J Suppl* **112** 199 (1997), T Rauscher *et al Phys Rev Lett* **C57** 2031 (1998)

[30] D L Lambert, V V Smith, N Busso, R Gallino and O Straniero *Astrophys. J.* **450** 302 (1995)

[31] H Beer and R L Macklin *Astrophys. J* **339** 962 (1989)

[32] R A Ward *Astrophys J* **216** 540 (1977)

[33] R A Ward and M J Newman *Astrophys J* **219** 195 (1978)

[34] R A Malaney *Astrophys Space Sci* **137** 251 (1987)

[35] H Beer, F Voss and R R Winters *Astrophys J Suppl* **80** 403 (1992)

[36] M Busso, G Picchio, R Gallino and A Chieffi *Astrophys J* **326** 196 (1988)

[37] M Busso, D L Lambert, L Beglio, R Gallino, C M Raiteri and V V Smith *Astrophys J* **446** 775 (1995)

[38] D L Lambert in *Proc of the IAU Symp 195 Evolution of Stars The Photospheric Abundance Connection* ed G Michard and A Tutukov (Dordrecht . Kluwer) p 299 (1991)

[39] T Blocker and D Schonberner in *Nuclei in the Cosmos* eds M Busso, R Gallino and C M Raiteri (New York · A I P) p 399 (1995)

[40] E A Lada, K M Strom and P C Myers in *Protostars an Planets III* eds. E H Levy and J I Lunine (USA University of Arizona Press) p 245 (1993)

[41] J Bally, J Morse and B Reipurth in *Science with the Hubble Space Telescope II* eds P Benvenuti, F D Macchette and E J Schreier (Space Telescope Sci. Institute; USA) (1996)

[42] R C Kennicutt Steward Observatory Preprint (1995)

[43] R C Kennicutt, F Bresolin, D J Bomans, G D Bothum and I B Thompson *Astrophys. J.* (1995) (Preprint)

[44] B S Meyer, W M Howard, C J Mathews, S E Woosley and R D Hoffman *Astrophys. J.* **399** 656 (1992)

[45] S E Woosley, J R Wilson, C J Mathews, R D Hoffman and B S Meyer *Astrophys. J.* **433** 229 (1994)

[46] D Ward-Thompson, P Andre and F Mott in *The Role of Dust in the Formation of Stars* eds U Kanfl and R Siebenmargen (in press)

[47] D Ward-Thompson and N E Jessop in *Proc of New Extragalactic Perspectives in the New South Africa Changing Perception of the Morphology Dust Content and Gas-Dust Ratios in Galaxies* (in press)

[48] J Bally, J Morse and B Reipurth in *Science with the Hubble Space Telescope II* eds P Benvenuti, F D Macchetto and E J Schreier (Space Telescope Sci Institute, USA) (1996)

[49] O G Benvenuti *Rev Mex Astron Astrophys* **2** 115 (1995)

[50] G F Ciolek and T Ch Mouschovias *Astrophys J* **425** 142 (1994)

[51] R B Larson in *Physical Processes in Fragmentation and Star Formation* eds R Capuzzo-Dolcetta *et al* (Dordrecht Kluwer) p 389 (1991)

[52] C J Lada and E A Lada in *The Formation and Evolution of Star Clusters* eds K James *et al* (San Francisco ASP) p 3 (1991)

[53] P C Myers and G A Fuller *Astrophys J* **402** 635 (1993)

[54] L Blitz in *The Physics of Star Formation and Early Stellar Evolution* eds C J Lada and N D Kylafis (Dordrecht Kluwer) (1991)

[55] S W Stahler, F H Shu and R E Taam *Astrophys J* **241** 637 (1980)

[56] S W Stahler, F H Shu and R E Taam *Astrophys. J* **248** 727 (1981)

[57] M Beech and R Mitalas *Astrophys J Suppl* **95** 517 (1994)

[58] J M Scalo *Fund Cosmic Phys* **11** 1 (1986)

[59] F Palla and S W Stahler *Astrophys J* **360** 147 (1990)

[60] F Palla and S W Stahler *Astrophys J* **375** 288 (1991)

[61] F Palla and S W Stahler *Astrophys J* **392** 667 (1992)

[62] H Sakai, H Okamura, N Matsuoka, A Shimizu, T Suda, M Ieiri and H M Shimizu *Nucl Phys* **A579** 45 (1994)

[63] H Oberhummer, H Herndl, T Rauscher and H Beer *Neutron Induced Nucleosynthesis* (1996) (preprint)

[64] P A Seeger, W A Fowler and D D Clayton *Astrophys J Suppl.* **11** 121 (1965)

[65] R Gallino, M Busso, C Arlandini M Lugaro and O Straniero *Mem Soc Astr It* (1996) (Preprint)

[66] R K Ulrich in *Proceedings of the Conference on Explosive Nucleosynthesis* eds D N Schramm and W D Arnett (Austin, USA Univ of Texas Press) p 139 (1973)

[67] R Gallino in *Evolution of Peculiar Red Giant Stars* eds H R Johnson and B Zuckerman (Cambridge, UK Cambridge University Press) p 176 (1989)

[68] R A Ward and M J Newman *Astrophys J* **219** 195 (1978)

[69] F Corvi, P Mutti, K Athanassopulos and H Beer in *AIP Conf Proceedings Nuclei in The Cosmos* eds M Busso, R Gallino and C M Raiteri (Am Inst Phys , USA) p 327 (1995)

[70] H Beer, F Corvi and P Mutti *Astrophys. J* **474** 843 (1997)

[71] S F Mughabghab, M Divadeenam and N E Holden *Neutron Cross Section* **1A** (New York Academic) (1981)

[72] R L Macklin, J Halperin and R R Winters *Astrophys J* **217** 222 (1977)

[73] D J Horen, C H Johnson, J L Fowler, A D MacKeller and B Castel *Phys Rev* **C34** 429 (1986)

[74] A R de Musgrone, B S Allen and P L Macklin *Aust. J. Phys.* **32** 213 (1979)

[75] T Rauscher, R Bieber, M Brozovic, H Oberhummer and J Dobaczewski *Phys Rev* **C 57** 2033 (1998)

[76] V Ratzel *Report KfK Karlsruhe* (1988) (unpublished)

[77] C Arlandini, R Gallino, M Busso and O Straniero in *Proc 32d Liege Int Astrophys Colloq* eds A Noels, D Fraipont-Caro, M Gabriel, N Grevesse and P Demarque (Liege: Univ Liege) p 447 (1996)

[78] R Gallino, M Busso, C Arlandini, M Lugaro and O Straniero *Mem Soc Astron Italiana* (1997) (preprint)

[79] T Rauscher, H Beer, H Oberhummer and F-K Thielemann in *Proc Int Conf Nuclear Data for Sci & Technology* eds G Reffo *et al* (Italian Physical Socy: Bologna) p 1587 (1998)

[80] K A Toukan, K Debus, F Kappeler and G Reffo *Phys Rev* **C51** 1540 (1995)

[81] K F Wisshak, I Voss, I Kappeler, K Guber, I Kazakov, N Kornilov, M Uhl and G Reffo *Phys Rev* **C52** 2762 (1995)

[82] S Jaag and I Kappeler *Astrophys J* **464** 874 (1996)

[83] P Koehler, R Spencer, R Winters, K Guber, J Harvey, N Hill and M Smith *Phys Rev* **C54** 1463 (1996)

[84] G Wallerstein, I Iben (Jr), P Parker, A M Boesgaard, G M Hale, A E Champagne, C A Barnes, F Kappeler, V V Smith, R D Hoffman, F X Timmes, C Sneden, R N Boyd, B S Meyer and D L Lambert *Rev Mod Phys* **69** 995 (1997)

[85] C Sneden, A McWilliam, G W Preston, J J Cowan, D L Burris and B J Armosky *Astrophys J* **467** 819 (1996)

[86] J J Cowan and D L Burris *Private Communication* (1997)

[87] A Burrows, J Hoyes and B Fryxell *Astrophys J* **450** 830 (1995)

[88] H T Janka and E Muller *Astrophys J Lett* **448** L109 (1995)

[89] W C Haxton, K Langanke, Y-Z Qian and P Vogel *Phys Rev Lett* **78** 2694 (1997)

[90] Y-Z Qian, W C Haxton, K Langanke and P Vogel *Phys Rev* **C55** 1532 (1997); S E Wooley, J R Wilson, G J Mathews, R D Hoffman and B S Meyer *Astrophys J* **433** 229 (1994)

[91] S E Woosley and R D Hoffman *Astrophys J* **395** 202 (1992)

[92] C Freiburghaus *Diploma Thesis* (Univ of Basel, Switzerland) (1995)

[93] S Richter, U Ott and F Begemann *Nature* **391** 261 (1998)

[94] M Bolte *Nature* **385** 205 (1997)

[95] R D Hoffman, S E Woosley and Y-Z Qian *Proc Nuclei in the Cosmos Nucl Phys* **A621** 397c (1997)

[96] J Gorres, H Herndl, I J Thompson and M Wiescher *Phys Rev* **C52** 2231 (1995)

[97] N Prantzos, M Hashimot and K Nomoto *Astron Astrophys* **234** 211 (1990)

[98] G R Caughlan, W A Fowler, M J Harris and B A Zimmerman *Atomic Data and Nucl Data Tables* **32** 197 (1985) [CFHZ85]

[99] G R Caughlan and W A Fowler *Atomic Data and Nucl Data Tables* **40** 283 (1988) [CF88]

[100] M Hashimoto *Prog Theor Phys* **94** 663 (1995)

[101] L Buchmann, R E Azuma, C A Barnes, J Humblet and K Langanke *Phys Rev* **C54** 393 (1996)

[102] L Buchmann *Astrophys J* **468** L127 (1996)

[103] C E Rolfs and W S Rodney *Cauldrons in the Cosmos* (Chicago: Cambridge Univ Press) (1988)

[104] F Kappeler, M Wiescher, U Giesen, J Gorres, I Baraffe, M El-Eid, C M Raiteri, M Busso, R Gallino, M Limongi and A Chieffi *Astrophys J* **437** 396 (1994)

[105] J Meissner, H Schatz, J Gorres, H Herndle and M Wiescher *Phys Rev* **C53** 459 (1996)

[106] H Oberhummer, H Herndle, R Hofinger and Y Yamamoto in *Proc Nuclear Astrophys* **MPIA/P9** eds W Hillebrandt and E Muller (Max Planck Institute fur Astrophys, Garching) p46 (1996)

[107] C Efstadis, L Buchmann, P M Endt, H Herndl and M Wiescher *Phys Rev* **C53** 475 (1996)

[108] K L Kratz, W Ziegert, W Hillebrandt and F K Thielemann *Astron Astrophys* **125** 381 (1983)

[109] G M Hale in *Ref [84]* p 1028 (1997)

O Aubert, N Prantzos and I Baraffe *Astron Astrophys.* **312** 845 (1996)

[111] G Meynet and M Arnould in *Nuclei in the Cosmos* eds F Kappeler and K Wisshak (Institute of Physics, Bristol, UK) p 503 (1993)

[112] D Arnett *Supernovae and Nucleosynthesis* (Princeton, NJ: Princeton Univ Press) (1996)

[113] K Nomoto, M Hashimoto, T Tsujimoto, F K Thielemann, N Kishimoto, Y Kubo and N Nakasato *Nucl. Phys* **A616** 79c (1997)

[114] H A Bethe and J R Wilson *Astrophys J.* **295** 14 (1985), J R Wilson, R W Mayle, S E Woosley and T Weaver *Ann. N Y Acad Sci* **470** 267 (1987); R W Mayle in *Supernovae* ed A G Petschek (New York: Springer) p 267 (1990)

[115] J Witti in *Proc 7th Workshop on Nuclear Astrophys* **MPIA/P7** (Max Planck Institute fur Astrophys, Garching, Germany) p 107 (1993)

[116] D K Duncan, J Primas, J M Rebull, A M Boesgaard, C P Deliyannis, J M Hobbs, J R King and S G Ryan *Astrophys J* **488** 338 (1997)

[117] K Cunha, D L Lambert, M Lemke, D R Gies and L C Roberts *Astrophys J* (in press)

[118] M Gai *J Phys* **G24** 1625 (1998), F Kikuchi, Y Nagai, T S Suzuki, T Shima, T Ku, M Igashira, A Mengoni and T Otsuka *Phys Rev* **C57** 2724 (1998)

[119] K Kar, S Chakravarti, A Roy and S Sarkar *J Phys* **G24** 1641 (1998), J Suhonen and O Civitarese *Phys Rep.* **300** 123 (1998)

[120] H Toki, H Shen, K Sumiyoshi, D Hirata, H Sugahara and I Tanihata *J Phys* **G24** 1479 (1998), L Satpathy and R C Nayak *J Phys* **G24** 1527 (1998)

R N Boyd *J Phys.* **G24** 1617 (1998), T Rauscher, R Bieber, H Oberhummer, K L Kratz, J Dobaczewski, P Moller and M M Sharma *Phys Rev* **C57** 2031 (1998)

About the Reviewer

R K Parui did his MSc and PhD in Physics from Manipur University. His field of specialization is Condensed Matter Physics and he is interested in the Condensed Matter Astrophysics of Neutron Stars, Pulsars, ISM and its related area. At present, he is working on the behaviour of Neutron Star's internal magnetic field, magnetic field of pulsar radio emission region, its role towards understanding the accretion disk structure, Inter Stellar Medium (ISM) and Bubble Dynamics.